

Citation: Shaik J, Uchida TK, Vyasarayani CP. Effect of delay on control of direct resonance of ships in beam waves using a proportional–derivative controller with delay. *Journal of Computational and Nonlinear Dynamics* 17(6): 061004, 2022. doi: 10.1115/1.4053561.

# Effect of delay on control of direct resonance of ships in beam waves using a proportional–derivative controller with delay

Junaidvali Shaik<sup>a</sup>, Thomas K. Uchida<sup>b,\*</sup>, C.P. Vyasarayani<sup>a</sup>

<sup>a</sup> Department of Mechanical and Aerospace Engineering, Indian Institute of Technology Hyderabad  
Kandi, Sangareddy 502285, Telangana, India

<sup>b</sup> Department of Mechanical Engineering, University of Ottawa  
161 Louis-Pasteur, Ottawa, Ontario, K1N 6N5, Canada

\* Address all correspondence to this author. E-mail address: tuchida@uottawa.ca

February 15, 2022

## Abstract

A harmonically excited, single-degree-of-freedom time-delay system with cubic and quintic nonlinearities is studied. This system describes the direct resonance of a ship with an actively controlled anti-roll tank (ART) that is subjected to beam waves. We consider low-, medium-, and high-freeboard ship models. A proportional–derivative (PD) controller with a constant time delay is assumed to operate the pump in the active ART system. The delay originates from the time required to pump fluid from one container to another, the inertia of large impeller blades and linkages, and the measurement and processing time of the roll sensing unit. The stability boundary of the system, in the parametric space of the control gain and the delay, is derived analytically from

the characteristic equation of the linearized system. We show that the area of the zero equilibrium region is inversely related to the derivative time constant of the PD controller; thus, we focus on a strictly proportional-gain controller. The spectral Tau method is used to identify the eigenvalues associated with the zero equilibrium, since the rightmost eigenvalues determine the system's robustness to perturbations in the initial conditions. We use the method of multiple scales and harmonic balance to obtain the global bifurcation diagram in the space of the applied frequency and the amplitude of the response. Numerical simulations verify our analytical expressions. Study of the dynamics, stability, and control of the roll motion of ships is critical to avoid dynamic instabilities and capsizing.

**Keywords:** bifurcation; control; Floquet theory; harmonic balance; ship; stability.

---

# 1 Introduction

Ships navigating heavy seas are susceptible to various types of wave excitation. The dynamic interaction between the ship and the waves may lead to dynamic instabilities, resulting in high-amplitude roll excitation and, in the worst case, capsizing. Compared to the pitch and yaw motions, the roll motion of a ship has the least amount of damping [1]. In addition to the potential for capsizing, rolling can cause sea sickness, obstruct crew work, and limit the ability to handle equipment on naval vessels. Therefore, it is crucial to study the dynamics, stability, and control of the roll motion of ships.

The roll dynamics of a ship can become unstable through two mechanisms: direct excitation and parametric excitation. *Direct excitation* is a consequence of sea waves that are incident upon the port side or starboard side of the ship, directly exciting the roll motion. Beam waves (approximately perpendicular to the ship's heading) and oblique waves can both cause direct excitation. If the frequency of the wave matches the roll natural frequency, direct resonance occurs and leads to high-amplitude roll motion. Ships are typically navigated perpendicular to waves to reduce direct excitation of the roll motion. *Parametric excitation* is a consequence of the inherent coupling between the pitch and roll motions of a ship. Head and follower waves (incident on the bow and stern, respectively) directly excite the pitch motion, as do oblique waves. If the pitching frequency becomes twice the roll natural frequency, the ship will undergo parametric resonance and the roll motion will be excited indirectly. In general, the presence of oblique waves will excite both the roll and pitch motions; however, the direct roll excitation frequency can be made to be sufficiently different from the roll natural frequency by adjusting the speed and heading of the ship. This navigational strategy can reduce the roll amplitude of the ship, provided it is operated far from the state of direct roll resonance. However, the amplitude and speed of waves in the ocean are not controlled, and there are limits to the range and rate at which a ship's speed can be adjusted.

If direct roll resonance cannot be controlled by adjusting the ship's speed, one can stabilize the roll motion via active control. Bilge keels, fins, rudders, gyroscopic stabilizers, and U-tube anti-roll tanks (ARTs) can be used to attenuate high-amplitude roll motions. Unlike the other control strategies, the performance of an ART is independent of the forward speed of the ship and thus is effective even when moored (e.g., to stabilize the ship while loading and unloading cargo). Additionally, the performance of an ART is independent of the natural frequency of the ship and the tank. A passive ART behaves like a tuned mass-damper system. An actively controlled ART pumps air between tanks on the port side and starboard side of the ship, displacing the water in the tanks and thereby generating torques that counter the ship's roll motion (Fig. 1). The time required to pump fluid from one tank to another, the inertia of the large impeller blades and linkages, and the measurement and processing time of the roll sensing unit are all sources of time delay in the correction-torque control system. Moving fluid from one tank to another has two effects: it changes the restoring arm of the ship by redistributing weight, and it changes the roll damping due to frictional losses of the fluid flow. Therefore, the ART can be modelled as a proportional-derivative (PD) feedback control system with time delay. In this work, we use theoretical and numerical techniques to investigate the nonlinear dynamics of ships undergoing direct resonance with active control in the presence of time delays. The mathematical model we consider is similar to models that arise in the study of other systems where delays are encountered, such as machine tool vibration [2], vibration of towed wheels [3], and delayed force control of robots [4].

In their pioneering work of the mid-1980s, Nayfeh and Khdeir [5, 6] studied the rolling of a ship as a single-degree-of-freedom nonlinear dynamical system and identified the existence of chaos when a ship is subjected to beam waves. In the 1990s, Thompson et al. [7, 8] identified the fractal structure in the safe-basin boundary of capsizing. Senjanović et al. [9] used a single-degree-of-freedom model to study the safe-basin boundary of capsizing for different values of sea state, ship speed, and wave direction. Many more analyses have been performed on the coupled

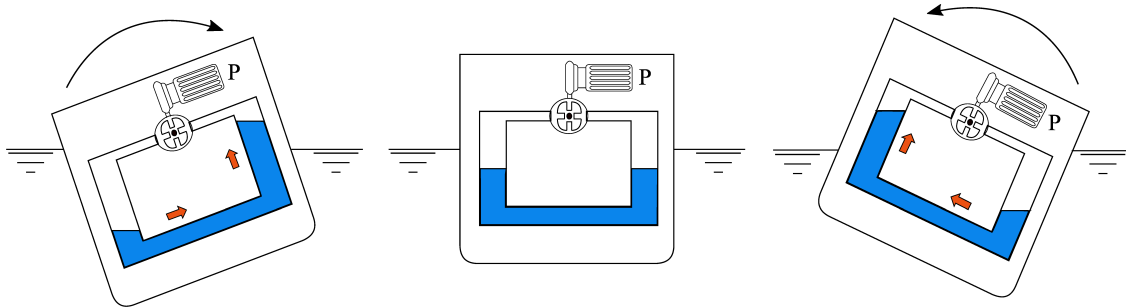


**Figure 1:** A ship equipped with an actively controlled anti-roll tank. The pump (P) pumps air between tanks to displace water (thick arrows) and generate corrective torques (curved arrows).

motion of ships to understand the dynamics of all six of their motions. Detailed literature reviews on the dynamics of ship motion have been published by Spyrou and Thompson [10], Spyrou [11], Ibrahim and Grace [12], and Neves [13].

Strategies to control the roll motion of a ship predate these analyses. In 1874, Froude [14] proposed a fluid-filled rectangular tank placed on the deck, above the ship's center of gravity. In 1885, Watts [15] proposed that, for best performance, the motion of the liquid inside the tank should be out of phase with the ship's rolling motion. Practical application of these tanks was unsuccessful due to the free surface effect and their use of valuable space on the deck. In 1911, Frahm [16] proposed a passive U-tube tank to overcome these disadvantages. The design consisted of two reservoirs connected with a horizontal pipe and was located below the ship's center of gravity.

In 1935, Minorsky [17] studied active control of a ship's rolling motion, considering nonlinear damping and a linear restoring moment. The control law was modelled based on the rate of rolling, which affects the roll damping. Minorsky highlighted the importance of delay; however, he neglected the higher-order terms in the Taylor series expansion of the delayed control function. In 1941, Minorsky [18] reviewed the state of the art at the time, including discussion on

the analysis of ship stability, rolling and pitching motions, and stabilization methods. In 1954, Chadwick and Klotter [19] studied the dynamics of a U-tube tank for United States Navy vessels. Stigter [20] and Van den Bosch and Vugts [21] analyzed the performance of various ART designs for the Netherlands Ship Research Center.

In 2001, Abdel Gawad et al. [22] considered a single passive U-tube ART to control the roll motion of a ship, using linear models for both the roll and fluid motions. The effects of tank damping, tank mass, and the location of the tank relative to the ship's center of gravity were analyzed. They concluded that a well-tuned passive ART can reduce roll amplitude effectively. Youssef et al. [23] extended this work and studied all six degrees of freedom of the ship; however, only the moments caused by fluid motion in the tank were considered. They investigated the effect of tank damping, frequency, and mass on the tank performance. In Youssef et al. [24], they compared the effectiveness of one, two, and three tanks, and concluded that a three-tank system was best for reducing roll.

In 2009, Marzouk and Nayfeh [25] extended the work of Youssef et al. by studying an active U-tank ART based on a proportional–derivative (PD) control law. They concluded that an active ART outperforms a passive ART in terms of roll reduction, size, and weight, and is more responsive to parametric rolling. Moaleji and Greig [26] proposed an active U-tank ART with a controller based on an adaptive inverse model. Numerous other studies have assessed the effect of both passive and active ARTs on a ship's roll motion [27, 28] and coupled roll-pitch-heave motions [29, 30].

The importance of feedback delays has been firmly established and remains a source of investigation (e.g., [31]). Spyrou [32] investigated the effect of heading and yaw rate feedback delays on the performance of a course-keeping controller, but no work in the existing literature has reported the effect of control system delays on the roll dynamics of a ship or on the performance of active U-tube ARTs. In this work, we model an actively controlled U-tube ART as a PD controller with constant delay. The delay originates from the time required for the fluid to be pumped from

one container to another, the inertia associated with large impeller blades and linkages, and the measurement and processing time of the roll sensing unit. We study the linear stability, normal forms near Hopf bifurcation points, and the response of the system under harmonic excitation. The presence of a delay results in an infinite-dimensional system, which makes the mathematical analysis challenging. We employ the method of multiple scales (MMS) [33], the method of harmonic balance [34], continuation techniques [35], and direct numerical simulation.

## 2 Mathematical Model

We consider a single-degree-of-freedom scaled model to study the relative rolling of a ship in a beam sea wave [5], with an added control function with time delay. This system is governed by the following equation:

$$\ddot{\phi}(t) + \omega_0^2\phi(t) + 2\hat{\mu}_1\dot{\phi}(t) + \hat{\mu}_3\dot{\phi}^3(t) + \hat{\alpha}_3\phi^3(t) + \hat{\alpha}_5\phi^5(t) = \hat{f}\cos(\omega_e t) + u(t - \tau), \quad (1)$$

where  $\phi(t)$  is the roll angle relative to the surface wave profile,  $\omega_0$  is the natural frequency,  $\hat{\mu}_1$  and  $\hat{\mu}_3$  are the linear and cubic damping coefficients,  $\hat{\alpha}_3$  and  $\hat{\alpha}_5$  are the coefficients of the restoring function, and  $\omega_e$  is the encounter frequency. Amplitude  $\hat{f}$  is proportional to the wave slope and is given as follows:

$$\hat{f} = \frac{F\omega_e}{I + \delta I}, \quad (2)$$

where  $F$  is the amplitude of the wave slope, which is defined as the angle between the wave surface and the horizontal plane or, equivalently, as the angle between the centerline plane of the ship and the vertical plane. For this analysis, we consider a unit roll moment of inertia ( $I$ ) and an added moment of inertia ( $\delta I$ ) amounting to 25% of the former. Finally, in Eq. (1),  $u(t - \tau)$  is the control function (with time delay  $\tau$ ) that corresponds to the effect of the ART. We consider a PD controller

for the subsequent analysis; thus, the governing equation (Eq. (1)) becomes the following:

$$\ddot{\phi}(t) + \omega_0^2 \phi(t) + 2\hat{\mu}_1 \dot{\phi}(t) + \hat{\mu}_3 \dot{\phi}^3(t) + \hat{\alpha}_3 \phi^3(t) + \hat{\alpha}_5 \phi^5(t) = \hat{f} \cos(\omega_e t) - \hat{k}_p \phi(t-\tau) - \hat{k}_d \dot{\phi}(t-\tau). \quad (3)$$

In the following analysis, we assume that  $\hat{k}_d = \rho \hat{k}_p$ , where  $\rho$  is called the derivative time constant.

The five fixed points of Eq. (3) when  $\hat{f} = 0$  are given by the following:

$$\bar{\phi} = 0, \quad \bar{\phi}^2 = -\frac{\hat{\alpha}_3}{2\hat{\alpha}_5} \pm \frac{\sqrt{\hat{\alpha}_3^2 - 4\hat{\alpha}_5 (\omega_0^2 + \hat{k}_p)}}{2\hat{\alpha}_5}. \quad (4)$$

The existence of five equilibrium points in our model is a consequence of the fifth-order approximation we have used for the restoring function. Nonzero equilibrium points exist only for  $\hat{k}_p \leq \frac{\hat{\alpha}_3^2}{4\hat{\alpha}_5} - \omega_0^2$ . This inequality indicates that there is a value for  $\hat{k}_p$  above which only the zero equilibrium point exists:  $\hat{k}_{p,\min} = \frac{\hat{\alpha}_3^2}{4\hat{\alpha}_5} - \omega_0^2$ . Because our objective is to control the roll motion of the ship around the zero equilibrium, we impose the condition  $\hat{k}_p \geq \hat{k}_{p,\min}$ , which ensures that only the zero equilibrium point exists in our model.

### 3 Linear Stability Analysis

Linear stability analysis is useful for studying the stability characteristics of a fixed point (here, the zero equilibrium point) in a parametric space of gains and delays. We first linearize Eq. (3) about the zero equilibrium point, then obtain the stability boundary analytically. Finally, the stable region in the parameter space of the proportional gain ( $\hat{k}_p$ ) and the delay ( $\tau$ ) is obtained using the spectral Tau method [36]. The stability boundary can be determined using several methods; the spectral Tau method is used here as it additionally provides information about the location of the rightmost eigenvalue of the system in the stable region.

Perturbing the homogeneous part of Eq. (3) about  $\bar{\phi} = 0$  using  $\phi(t) = r(t) + \bar{\phi}$ , we obtain the

following:

$$\ddot{r}(t) + \omega_0^2 r(t) + 2\hat{\mu}_1 \dot{r}(t) + \hat{\mu}_3 \dot{r}^3(t) + \hat{\alpha}_3 r^3(t) + \hat{\alpha}_5 r^5(t) + \hat{k}_p [r(t - \tau) + \rho \dot{r}(t - \tau)] = 0. \quad (5)$$

Retaining only the linear terms in Eq. (5) and substituting the solution  $r(t) = Ce^{\lambda t}$ , where  $\{C, \lambda\} \in \mathbb{C}^2$ , we arrive at the following characteristic equation:

$$D(\lambda) = \lambda^2 + 2\hat{\mu}_1\lambda + \omega_0^2 + \hat{k}_p e^{-\lambda\tau} (1 + \rho\lambda). \quad (6)$$

This is a quasi-polynomial and, thus, has an infinite number of roots. The homogeneous solution is asymptotically stable if all the eigenvalues lie on the left half of the complex plane; it is at the stability boundary if the rightmost eigenvalue is at the origin or if there exists a pair of complex conjugate eigenvalues of the form  $\lambda = \pm j\omega_{cr}$  (where  $j^2 = -1$  and  $\omega_{cr} > 0$ ). Finally, the homogeneous solution is unstable if at least one of the real eigenvalues is positive or if there exists a pair of complex conjugate eigenvalues whose real part is positive. Note that  $\lambda = \pm j\omega_{cr}$  corresponds to a Hopf bifurcation. Therefore, Hopf bifurcation points can be found by substituting  $\lambda = j\omega_{cr}$  (or  $\lambda = -j\omega_{cr}$ ) into Eq. (6) and separating the result into its real and imaginary parts:

$$\Re \{D(j\omega_{cr})\} = \hat{k}_p \cos(\omega_{cr}\tau) + \hat{k}_p \rho \omega_{cr} \sin(\omega_{cr}\tau) - \omega_{cr}^2 + \omega_0^2, \quad (7a)$$

$$\Im \{D(j\omega_{cr})\} = \hat{k}_p \rho \omega_{cr} \cos(\omega_{cr}\tau) - \hat{k}_p \sin(\omega_{cr}\tau) + 2\hat{\mu}_1 \omega_{cr}. \quad (7b)$$

Linear stability boundaries can now be obtained by solving Eq. (7) for  $\hat{k}_p$  and  $\tau$ :

$$\hat{k}_p = \frac{\sqrt{(1 + \rho^2 \omega_{cr}^2) \left(4\hat{\mu}_1^2 \omega_{cr}^2 + (\omega_{cr}^2 - \omega_0^2)^2\right)}}{1 + \rho^2 \omega_{cr}^2}, \quad (8a)$$

$$\tau = \frac{2}{\omega_{cr}} \left[ n\pi + \arctan \left( \frac{\sqrt{(1 + \rho^2 \omega_{cr}^2) \left(4\hat{\mu}_1^2 \omega_{cr}^2 + (\omega_{cr}^2 - \omega_0^2)^2\right)} + \omega_{cr}^2 (2\rho\hat{\mu}_1 - 1) + \omega_0^2}{\rho \omega_{cr} (\omega_{cr}^2 - \omega_0^2) + 2\hat{\mu}_1 \omega_{cr}} \right) \right]. \quad (8b)$$

Equation (8) describes a family of curves, called stability lobes, where  $n$  is the lobe number.

**Table 1:** Parameter values for the models of Wright and Marshfield [37] (obtained from Nayfeh and Khdeir [5]), and the relative roll angle (in radians) at the maximum restoring moment before capsizing ( $\phi_{cr}$ ).

	$\omega_0$	$\hat{\alpha}_3/\omega_0^2$	$\hat{\alpha}_5/\omega_0^2$	$\hat{\mu}_1$	$\hat{\mu}_3$	$\phi_{cr}$
Low freeboard	5.2779	-1.69119	0.63297	0.0855	0.108	0.48
Medium freeboard	5.2779	-0.71455	0.11342	0.090	0.096	0.74
High freeboard	4.790	-0.32651	0.01140	0.0735	0.094	1.04

In the following numerical analysis, we consider the low-, medium-, and high-freeboard models of Wright and Marshfield [37]. The parameters for these models are provided in Table 1 [5, 37], along with the relative roll angle at the maximum restoring moment before capsizing ( $\phi_{cr}$ ). The angle  $\phi_{cr}$  was obtained by plotting the nonlinear restoring function as a function of the relative roll angle. Equation (8) was used to generate stability diagrams in the parametric space of the proportional gain ( $\hat{k}_p$ ) and the delay ( $\tau$ ), with  $\rho = 0$ , as shown in Fig. 2(a–c). The horizontal dashed line labelled  $\hat{k}_{p,\min}$  represents the minimum gain required to avoid stable limit cycle oscillations; the region above the dashed line (i.e.,  $\hat{k}_p > \hat{k}_{p,\min}$ ) is the operating region for zero equilibrium. As shown in Fig. 2(c), the high-freeboard model does not have a stable region of the zero equilibrium within the operating region. To determine the optimal control parameters in this case, we would require additional information about the nonzero equilibrium points which is beyond the scope of the current work. Thus, we consider only the low- and medium-freeboard models in the analysis that follows.

Figure 2(d) illustrates the area of the stable region ( $\eta$ ) as a function of the derivative time constant ( $\rho$ ). (Recall that  $\hat{k}_d = \rho\hat{k}_p$ .) The area of the stable region is obtained via numerical integration from the  $(\hat{k}_p, \tau)$  data (e.g., the regions shown in Figs. 2(a) and 2(b) for  $\rho = 0$ ) for

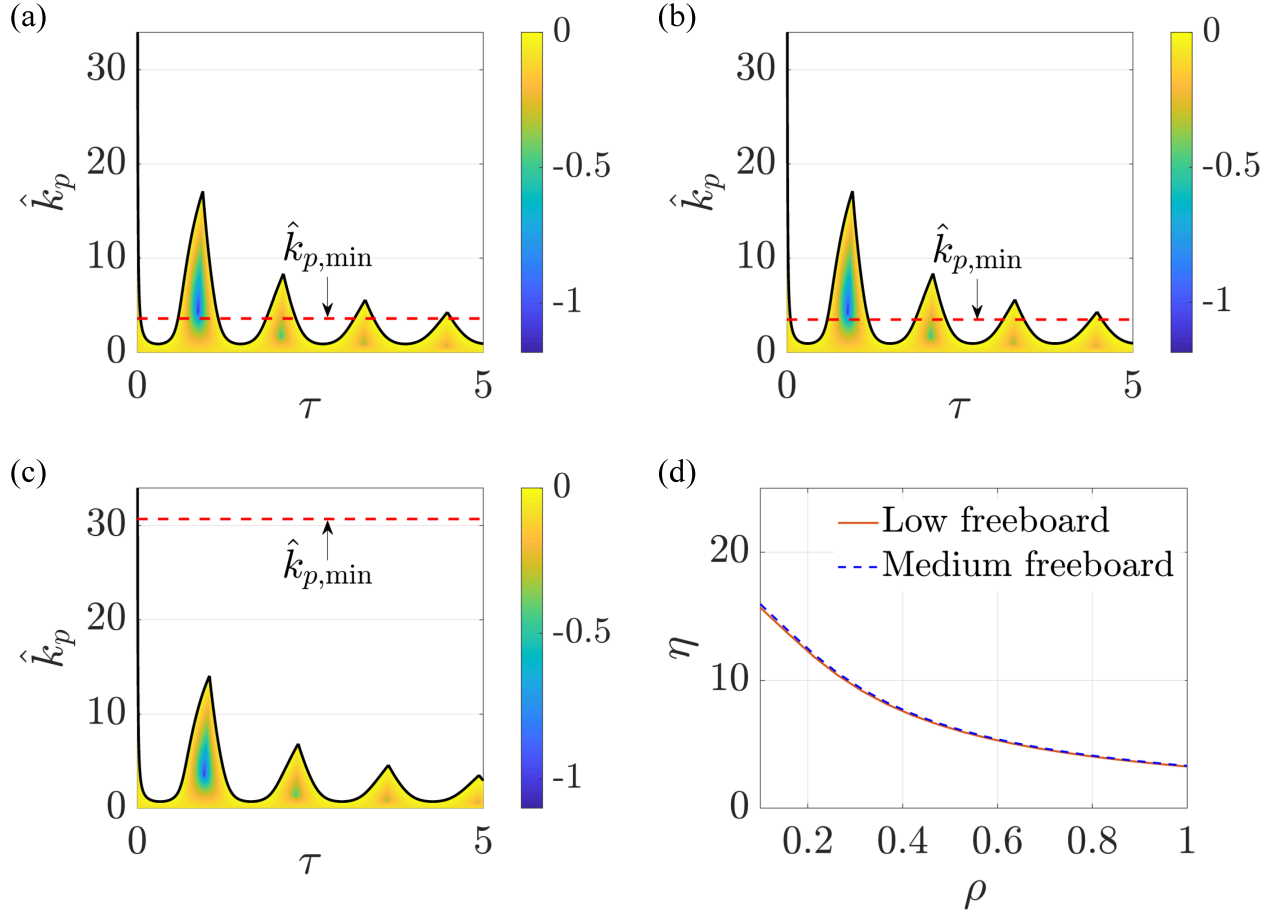


**Figure 2:** Linear stability charts and rightmost eigenvalue contours for (a) low-freeboard, (b) medium-freeboard, and (c) high-freeboard models (all with  $\rho = 0$ ); and (d) the relationship between the area of the stability region ( $\eta$ ) and the derivative time constant ( $\rho$ ) for low- and medium-freeboard models. A delay of  $\tau = 5$  s corresponds to approximately 4 times the period of natural oscillation for the low- and medium-freeboard models.

different values of  $\rho$ . Note that, for both the low-freeboard and medium-freeboard models, the area of the stable region decreases as  $\rho$  increases. We, therefore, conclude that the derivative term is detrimental to the stability of this system and proceed only with the proportional-gain controller.

To determine the optimal values for the proportional gain ( $\hat{k}_p$ ) and delay ( $\tau$ ) parameters in the control function, we consider the location of the rightmost eigenvalue. In particular, the rightmost eigenvalue should be as far from the imaginary axis as possible, which corresponds to the greatest robustness to perturbations in the initial conditions [38]. We use the spectral Tau method to compute the rightmost eigenvalues of the linear delay differential equation (DDE) given by Eq. (5) (after dropping the higher-order terms). Figures 2(a) and 2(b) show contour plots of the rightmost eigenvalue locations for the low- and medium-freeboard models in the parametric space. The optimal gain and delay are  $\hat{k}_p = 4.23 \text{ s}^{-2}$  and  $\tau = 0.87 \text{ s}$  for the low-freeboard model, and  $\hat{k}_p = 4.21 \text{ s}^{-2}$  and  $\tau = 0.87 \text{ s}$  for the medium-freeboard model. (In the figures, these points are shown in the darkest blue colour.) Note, however, that these parameters are not universally optimal for the control function, as we considered only the linearized system around the zero equilibrium; due to nonlinearities, these parameters may fail to control the roll amplitude effectively at high values of the wave slope. In Sections 6 and 7, these parameters will be used to analyze the system under harmonic excitation.

## 4 Local Bifurcation Analysis and Normal Forms

The normal forms of a dynamical system are useful for performing a local bifurcation analysis and for obtaining qualitative insights into the system behaviour at bifurcation points. The method of center manifold reduction [39] is generally used to obtain the normal forms. However, we can apply the method of multiple scales (MMS) [40] to Eq. (5) to obtain the normal-form equations at the Hopf bifurcation points. We introduce a bookkeeping parameter  $\epsilon$  and let  $\hat{\mu}_3 = \epsilon\mu_3$ ,  $\hat{\alpha}_3 = \epsilon\alpha_3$ ,

$\hat{\alpha}_5 = \epsilon\alpha_5$ ,  $\hat{k}_p = k_{cr} + \epsilon\delta$ , and  $\rho = 0$ . Upon substituting these values into Eq. (5), we obtain the following:

$$\ddot{r}(t) + 2\hat{\mu}_1\dot{r}(t) + \omega_0^2 r(t) + k_{cr}r(t - \tau) + \epsilon [\delta r(t - \tau) + \mu_3\dot{r}^3(t) + \alpha_3r^3(t) + \alpha_5r^5(t)] = 0. \quad (9)$$

For  $\epsilon = 0$ , Eq. (9) is simply a linear DDE with damping. Here, we are perturbing the linear DDE and using the MMS approach to obtain the normal-form equations at the Hopf bifurcation points—that is, for  $\lambda = \pm j\omega_{cr}$ . Once the transients have died out, the response will be of the following form:

$$r(t) = A \sin(\omega_{cr}t) + B \cos(\omega_{cr}t). \quad (10)$$

The solution to Eq. (9) is assumed to be of the following form:

$$r(t) = r_0(T_0, T_1, T_2) + \epsilon r_1(T_0, T_1, T_2) + \epsilon^2 r_2(T_0, T_1, T_2), \quad (11)$$

where three time scales (i.e.,  $T_0$ ,  $T_1$ , and  $T_2$ ) have been retained and  $T_i = \epsilon^i t, i \in \{0, 1, 2\}$ . Substituting Eq. (11) into Eq. (9), collecting the coefficients of like powers of  $\epsilon$ , and equating each to zero, we obtain the following:

$$\mathcal{O}(\epsilon^0) : D_0^2 r_0(T_0, T_1, T_2) + 2\hat{\mu}_1 D_0 r_0(T_0, T_1, T_2) + \omega_0^2 r_0(T_0, T_1, T_2) + k_{cr} r_0(T_0 - \tau, T_1, T_2) = 0, \quad (12)$$

$$\begin{aligned} \mathcal{O}(\epsilon^1) : & D_0^2 r_1(T_0, T_1, T_2) + 2D_0 D_1 r_0(T_0, T_1, T_2) + \omega_0^2 r_1(T_0, T_1, T_2) + 2\hat{\mu}_1 [D_0 r_1(T_0, T_1, T_2) \\ & + D_1 r_0(T_0, T_1, T_2)] + \mu_3 [D_0 r_0(T_0, T_1, T_2)]^3 + \alpha_3 r_0(T_0, T_1, T_2)^3 + \alpha_5 r_0(T_0, T_1, T_2)^5 \\ & - k_{cr} [\tau D_2 r_0(T_0 - \tau, T_1, T_2) - r_1(T_0 - \tau, T_1, T_2)] + \delta r_0(T_0 - \tau, T_1, T_2) = 0, \end{aligned} \quad (13)$$

where  $D_n \triangleq \partial/\partial T_n$ . The solution of Eq. (12) can be expressed in the following form:

$$r_0(T_0, T_1, T_2) = A(T_1, T_2) \sin(\omega_{cr}T_0) + B(T_1, T_2) \cos(\omega_{cr}T_0). \quad (14)$$

The functions  $A(T_1, T_2)$  and  $B(T_1, T_2)$  are determined by applying the solvability conditions (i.e., eliminating the secular terms, or the terms that cause resonance in a solution) on the next-order approximation. Substituting Eq. (14) into Eq. (13), we obtain the following:

$$\begin{aligned} & D_0^2 r_1(T_0, T_1, T_2) + \omega_0^2 r_1(T_0, T_1, T_2) + 2\hat{\mu}_1 D_0 r_1(T_0, T_1, T_2) + k_{cr} r_1(T_0 - \tau, T_1, T_2) \\ & + P_1 \cos(\omega_{cr} T_0) + P_2 \sin(\omega_{cr} T_0) + P_3 \cos(3\omega_{cr} T_0) + P_4 \sin(3\omega_{cr} T_0) \\ & + P_5 \cos(5\omega_{cr} T_0) + P_6 \sin(5\omega_{cr} T_0) = 0. \end{aligned} \quad (15)$$

In Eq. (15), the variables  $P_i$  are given as follows:

$$\begin{aligned} P_1 = & \frac{5}{8}\alpha_5 B^5 + \left(\frac{5}{4}\alpha_5 A^2 + \frac{3}{4}\alpha_3\right) B^3 + \frac{3}{4}\mu_3\omega_{cr}^3 AB^2 + \left(\frac{5}{8}\alpha_5 A^2 + \frac{3}{4}\alpha_3\right) A^2 B + \frac{3}{4}\mu_3\omega_{cr}^3 A^3 \\ & + 2\hat{\mu}_1 D_1 B + 2\omega_{cr} D_1 A - (k_{cr}\tau D_1 B - \delta B) \cos(\omega_{cr}\tau) + (k_{cr}\tau D_1 A - \delta A) \sin(\omega_{cr}\tau), \end{aligned} \quad (16a)$$

$$\begin{aligned} P_2 = & \frac{5}{8}\alpha_5 A^5 + \left(\frac{5}{4}\alpha_5 B^2 + \frac{3}{4}\alpha_3\right) A^3 - \frac{3}{4}\mu_3\omega_{cr}^3 BA^2 + \left(\frac{5}{8}\alpha_5 B^2 + \frac{3}{4}\alpha_3\right) B^2 A - \frac{3}{4}\mu_3\omega_{cr}^3 B^3 \\ & + 2\hat{\mu}_1 D_1 A - 2\omega_{cr} D_1 B - (k_{cr}\tau D_1 A - \delta A) \cos(\omega_{cr}\tau) - (k_{cr}\tau D_1 B - \delta B) \sin(\omega_{cr}\tau), \end{aligned} \quad (16b)$$

$$P_3 = \frac{5}{16}\alpha_5 B^5 - \left(\frac{5}{8}\alpha_5 A^2 - \frac{1}{4}\alpha_3\right) B^3 - \frac{3}{4}\mu_3\omega_{cr}^3 AB^2 - \left(\frac{15}{16}\alpha_5 A^2 + \frac{3}{4}\alpha_3\right) A^2 B + \frac{1}{4}\mu_3\omega_{cr}^3 A^3, \quad (16c)$$

$$P_4 = -\frac{5}{16}\alpha_5 A^5 + \left(\frac{5}{8}\alpha_5 B^2 - \frac{1}{4}\alpha_3\right) A^3 - \frac{3}{4}\mu_3\omega_{cr}^3 BA^2 + \left(\frac{15}{16}\alpha_5 B^2 + \frac{3}{4}\alpha_3\right) B^2 A + \frac{1}{4}\mu_3\omega_{cr}^3 B^3, \quad (16d)$$

$$P_5 = \frac{1}{16}\alpha_5 B^5 - \frac{5}{8}\alpha_5 A^2 B^3 + \frac{5}{16}\alpha_5 A^4 B, \quad (16e)$$

$$P_6 = \frac{1}{16}\alpha_5 A^5 - \frac{5}{8}\alpha_5 B^2 A^3 + \frac{5}{16}\alpha_5 B^4 A, \quad (16f)$$

where  $A(T_1, T_2)$  and  $B(T_1, T_2)$  have been replaced with  $A$  and  $B$ , respectively.  $D_1 A$  and  $D_1 B$  can be obtained by solving  $P_1 = 0$  and  $P_2 = 0$ ; the resulting expressions are lengthy and are omitted

here for brevity. Finally, the equations to compute the time derivatives of  $A$  and  $B$  are given as follows:

$$\frac{dA}{dt} = \epsilon \frac{\partial A}{\partial T_1} + \mathcal{O}(\epsilon^2), \quad (17a)$$

$$\frac{dB}{dt} = \epsilon \frac{\partial B}{\partial T_1} + \mathcal{O}(\epsilon^2). \quad (17b)$$

Here, we are limiting the analysis to the first order only as this will be sufficient for the local bifurcation analysis. To simplify Eq. (17), we express  $A$  and  $B$  in polar coordinates:

$$A(T_1, T_2) = a(t) \cos(\beta(t)), \quad (18a)$$

$$B(T_1, T_2) = a(t) \sin(\beta(t)). \quad (18b)$$

Solving for  $\dot{a}(t)$  and  $\dot{\beta}(t)$ , we obtain the following:

$$\dot{a} = \frac{1}{E} (N_1 a^5 + N_2 a^3 + N_3 a), \quad (19a)$$

$$\dot{\beta} = \frac{1}{E} (N_4 a^4 + N_5 a^2 + N_6), \quad (19b)$$

where  $a \triangleq a(t)$  and  $\beta \triangleq \beta(t)$  for brevity, and

$$N_1 = 5\hat{\alpha}_5 [k_{cr}\tau \cos(\omega_{cr}\tau) - 2\hat{\mu}_1], \quad (20a)$$

$$N_2 = 6 \left\{ k_{cr}\tau [\hat{\alpha}_3 \cos(\omega_{cr}\tau) - \hat{\mu}_3 \omega_{cr}^3 \sin(\omega_{cr}\tau)] - 2\hat{\mu}_3 \omega_{cr}^4 - 2\hat{\alpha}_3 \hat{\mu}_1 \right\}, \quad (20b)$$

$$N_3 = 8\epsilon\delta [k_{cr}\tau + 2\omega_{cr} \sin(\omega_{cr}\tau) - 2\hat{\mu}_1 \cos(\omega_{cr}\tau)], \quad (20c)$$

$$N_4 = 5\hat{\alpha}_5 [k_{cr}\tau \sin(\omega_{cr}\tau) + 2\omega_{cr}], \quad (20d)$$

$$N_5 = 6 \left\{ \hat{\mu}_3 \omega_{cr}^3 [k_{cr}\tau \cos(\omega_{cr}\tau) - 2\hat{\mu}_1] + k_{cr}\tau \hat{\alpha}_3 \sin(\omega_{cr}\tau) + 2\hat{\alpha}_3 \omega_{cr} \right\}, \quad (20e)$$

$$N_6 = 16\epsilon\delta [\omega_{cr} \cos(\omega_{cr}\tau) + \hat{\mu}_1 \sin(\omega_{cr}\tau)], \quad (20f)$$

$$E = 32k_{cr}\tau [\omega_{cr} \sin(\omega_{cr}\tau) - \hat{\mu}_1 \cos(\omega_{cr}\tau)] + 8k_{cr}^2 \tau^2 + 32 (\hat{\mu}_1^2 + \omega_{cr}^2). \quad (20g)$$

We present numerical results obtained at an arbitrarily selected critical frequency ( $\omega_{cr}$ ) and stability lobe number ( $n$ ); we choose  $\omega_{cr} = 6$  rad/s and  $n = 1$ . The corresponding Hopf bifurcation

point for the low-freeboard model is given by  $k_{cr} = 8.208 \text{ s}^{-2}$  and  $\tau = 1.068 \text{ s}$ . At the bifurcation point, the averaged equations (normal forms) approximate the actual system response; hence, the averaged equations are used locally for a qualitative analysis of the system. Substituting the parameters for the low-freeboard model from Table 1 into Eq. (19), we obtain the following system:

$$\dot{a}(t) = 0.385a^5(t) - 2.172a^3(t) + 0.041(\epsilon\delta)a(t), \quad (21a)$$

$$\dot{\beta}(t) = 0.591a^4(t) - 1.284a^2(t) + 0.049(\epsilon\delta). \quad (21b)$$

The numerical calculations are unstable near the bifurcation points; thus, it is highly advantageous to analyze the fixed points ( $a^*$ ) of Eq. (21) at the bifurcation points:

$$a^* = \left\{ 0, \pm \sqrt{2.822 \pm \sqrt{7.965 - 0.107\epsilon\delta}} \right\}. \quad (22)$$

We can conclude from Eq. (22) that multiple solutions exist for the system: nonzero real fixed points (which are equivalent to limit cycles) are evident for  $\epsilon\delta < 74.4$ . However, for local bifurcation analysis, we impose the restriction that  $\epsilon\delta \in [-1, 1]$ . An analogous analysis can be performed for the medium-freeboard model, where the slow-flow equations and fixed points at  $k_{cr} = 8.215 \text{ s}^{-2}$  and  $\tau = 1.069 \text{ s}$  (again for  $\omega_{cr} = 6 \text{ rad/s}$  and  $n = 1$ ) are as follows:

$$\dot{a}(t) = 0.068a^5(t) - 1.350a^3(t) + 0.041(\epsilon\delta)a(t), \quad (23a)$$

$$\dot{\beta}(t) = 0.106a^4(t) - 0.260a^2(t) + 0.048(\epsilon\delta), \quad (23b)$$

$$a^* = \left\{ 0, \pm \sqrt{9.856 \pm \sqrt{97.135 - 0.605\epsilon\delta}} \right\}. \quad (24)$$

Numerical results for the low- and medium-freeboard models are summarized in Figs. 3 and 4, respectively. The “dde23” solver in MATLAB® is used to compute the time response of the system, with absolute and relative tolerances set to  $10^{-6}$ . The slow-flow equations (Eqs. (21) and (23)) are solved by specifying initial conditions  $a(0)$  and  $\beta(0)$ ; the resulting solutions in the range

$0 \leq t \leq \tau$  are then used as the history functions when solving the DDE system. Figure 3(a) shows the response of the low-freeboard system (with delay  $\tau = 1.068$  s) for proportional gains around the critical gain  $k_{cr} = 8.208 \text{ s}^{-2}$ . These results indicate the presence of a supercritical Hopf bifurcation at  $k_{cr}$ . For a physical interpretation, consider the dynamics of a ship around the Hopf bifurcation point in a calm sea. In the pre-bifurcation regime (i.e., for  $\epsilon\delta < 0$ ), the ship will attenuate a small disturbance, such as a low-amplitude wave, and return to zero equilibrium. An example of this is shown in Fig. 3(b) for  $\epsilon\delta = -0.5$ . In contrast, in the post-bifurcation regime (i.e., for  $\epsilon\delta > 0$ ), the ship will exhibit limit-cycle oscillations when subjected to small disturbances, as shown in Fig. 3(c) for  $\epsilon\delta = 0.5$ . The results shown in Figs. 3(b) and 3(c) were generated by simulating the system (Eq. (21)) with an initial roll amplitude of 0.2. The fixed points ( $a^*$ ) given by Eqs. (22) and (24) provide qualitative information about the existence of a high-amplitude limit cycle in the pre-bifurcation regime, and both low- and high-amplitude limit cycles in the post-bifurcation regime. In the next section, we use numerical methods to verify these observations via a global bifurcation analysis. Analogous observations can be drawn from Fig. 4 for the medium-freeboard model. Figures 3 and 4 indicate agreement between our analytical approximations using the method of multiple scales and our numerical solutions using the “dde23” solver.

## 5 Global Bifurcation Analysis

In Section 4, we inferred the existence of high-amplitude limit cycles in addition to the zero equilibrium from the fixed points of the slow-flow equations (Eqs. (22) and (24)). The slow-flow equations are only valid locally; thus, we cannot use them for a global analysis. Here, we use the “dde23” solver to perform a global analysis, solving Eq. (9) directly. A constant roll angle is used as the history function for  $r(t)$ ; the history function for  $\dot{r}(t)$  is zero. The amplitudes of the unstable limit cycles are found using the bisection method. Absolute and relative tolerances are set to  $10^{-6}$

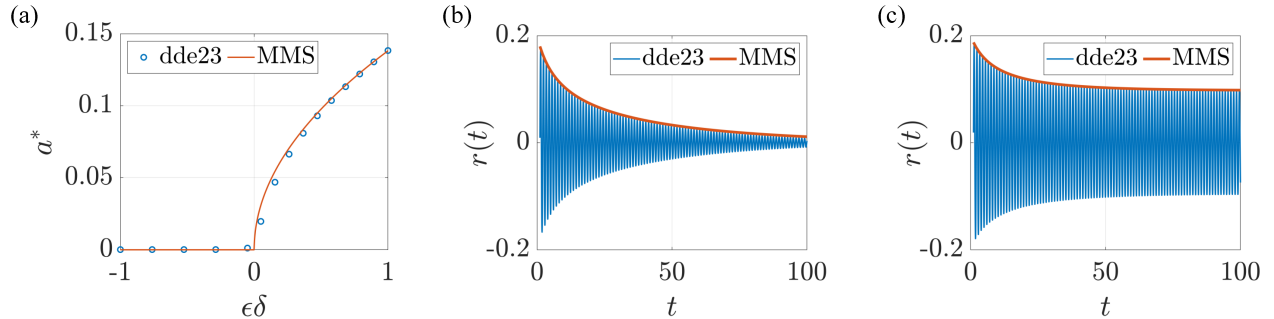


**Figure 3:** Numerical results for low-freeboard ship model where  $\omega_{cr} = 6$  rad/s,  $n = 1$ ,  $k_{cr} = 8.208$  s $^{-2}$ , and  $\tau = 1.068$  s: (a) local bifurcation diagram, (b) comparison of system response obtained using the “dde23” solver and the method of multiple scales (MMS) for  $\epsilon\delta = -0.5$ , and (c) the same for  $\epsilon\delta = 0.5$ .

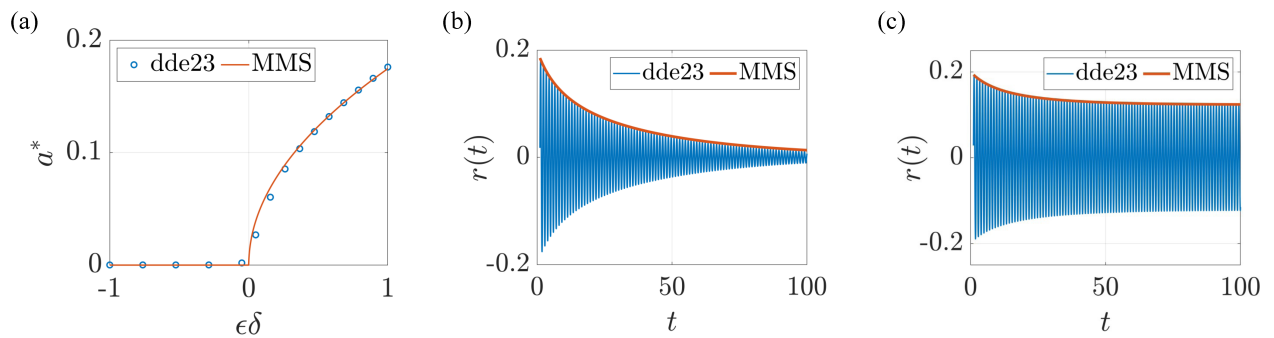


**Figure 4:** Numerical results for medium-freeboard ship model where  $\omega_{cr} = 6$  rad/s,  $n = 1$ ,  $k_{cr} = 8.215$  s $^{-2}$ , and  $\tau = 1.069$  s: (a) local bifurcation diagram, (b) comparison of system response obtained using the “dde23” solver and the method of multiple scales (MMS) for  $\epsilon\delta = -0.5$ , and (c) the same for  $\epsilon\delta = 0.5$ .

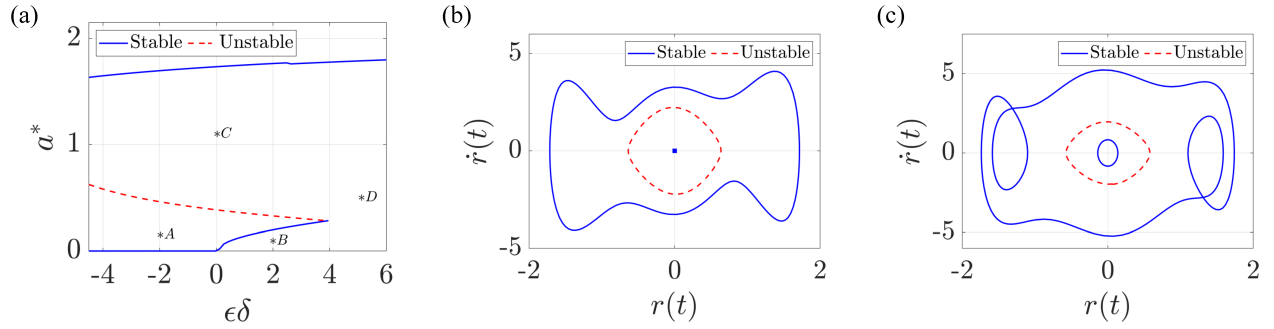


**Figure 5:** Global bifurcation analysis for the low-freeboard model: (a) global bifurcation diagram, (b) phase-plane diagram for  $\epsilon\delta = -1$ , and (c) phase-plane diagram for  $\epsilon\delta = 1$ .

throughout.

The global bifurcation diagrams and phase plane analysis at the Hopf bifurcation points are shown in Fig. 5 for the low-freeboard model. The global bifurcation analyses are consistent with the local bifurcation analyses of Section 4 in the vicinity of the Hopf bifurcation points. To interpret the results of the global bifurcation analyses, we consider initial conditions in various regions of the phase plane, labelled *A*, *B*, *C*, and *D* in Fig. 5(a). In the pre-bifurcation regime at *A* (i.e., where  $\epsilon\delta = -2$  and the initial roll amplitude is 0.2), disturbances will die out. In contrast, if the system begins in the region to the left of *C*, a disturbance will lead the system to high-amplitude limit cycles. Moreover, since the amplitude of the limit cycle exceeds the critical roll angle, the ship will capsize under such conditions. In the post-bifurcation regime, the system exhibits limit-cycle oscillations without capsizing up to  $\epsilon\delta = 4$ , provided the disturbance is within the regime of stable limit cycles (e.g., at *B*). For initial conditions beyond this limit (e.g., in the region to the right of *C*), the system performs period-doubling capsizing limit cycles. Finally, for  $\epsilon\delta > 4$  (e.g., at *D*), the system evolves directly to period-doubling capsizing limit cycles—that is, the ship will immediately capsize upon the slightest disturbance.

Similar observations can be made for the results with the medium-freeboard model, shown in

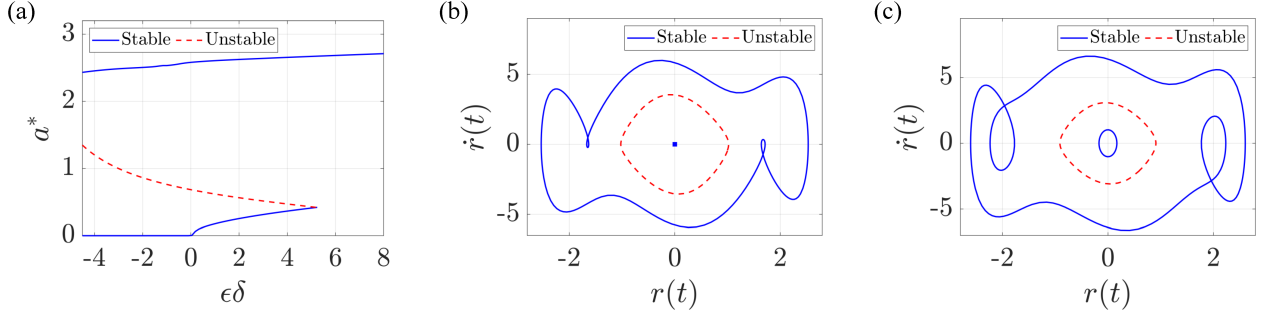


**Figure 6:** Global bifurcation analysis for the medium-freeboard model: (a) global bifurcation diagram, (b) phase-plane diagram for  $\epsilon\delta = -1$ , and (c) phase-plane diagram for  $\epsilon\delta = 1$ .

Fig. 6. By comparison, the medium-freeboard model exhibits limit cycles of higher amplitude than those of the low-freeboard model.

## 6 Forced Response using Method of Multiple Scales

The forced response of the system refers to its response under external forcing with zero initial conditions. In this section, we analyze the dynamics of the ship when subjected to a beam sea wave, which acts as the external forcing. For this forced response analysis, we operate the control system at the optimal proportional gain and delay (see Section 3). The optimal proportional gain and delay for the low-freeboard model are  $\hat{k}_p = 4.23 \text{ s}^{-2}$  and  $\tau = 0.87 \text{ s}$ , and for the medium-freeboard model are  $\hat{k}_p = 4.21 \text{ s}^{-2}$  and  $\tau = 0.87 \text{ s}$ .

In practice, it is important to determine the maximum amplitude of the wave slope that a ship can sustain when the optimal ART parameters are used. We use the method of multiple scales (MMS) to study the response of the harmonically excited system by finding closed-form solutions. We introduce a bookkeeping parameter  $\epsilon$ , similar to that defined in Section 4. For the primary resonance analysis, the difference between the encounter frequency  $\omega_e$  and the natural frequency

$\omega_0$  is defined using a detuning parameter  $\sigma$ :

$$\omega_e = \omega_0 + \epsilon\sigma. \quad (25)$$

For linear undamped systems, a forcing function with  $\sigma = 0$  results in an unbounded response regardless of the amplitude of the excitation. In most practical systems, the response will be bounded as a result of damping and nonlinearity.

To apply MMS, we perturb the linear undamped system; specifically, we place the force with nonlinearity and damping in the same order. We assume the existence of a weak nonlinearity, small damping, and a weak but near-resonant forcing. First, we include the forcing term  $\hat{f} \cos(\omega_e t)$  (refer to Eq. (3)) in Eq. (5) and substitute  $\hat{\mu}_1 = \epsilon\mu_1$ ,  $\hat{\mu}_3 = \epsilon\mu_3$ ,  $\hat{\alpha}_3 = \epsilon\alpha_3$ ,  $\hat{\alpha}_5 = \epsilon\alpha_5$ ,  $\hat{k}_p = \epsilon k$ ,  $\rho = 0$ ,  $\hat{f} = \epsilon f$ , and  $\omega_e = \omega_0 + \epsilon\sigma$ :

$$\ddot{r}(t) + \omega_0^2 r(t) + \epsilon [2\mu_1 \dot{r}(t) + \mu_3 \dot{r}^3(t) + \alpha_3 r^3(t) + \alpha_5 r^5(t) + kr(t - \tau) - f \cos(\omega_0 t + \epsilon\sigma t)] = 0. \quad (26)$$

To apply MMS, we define time scales  $T_i = \epsilon^i t$ ,  $i \in \{0, 1, 2\}$  and retain the first three terms. The solution to Eq. (26) is assumed to be of the following form:

$$r(t) = r_0(T_0, T_1, T_2) + \epsilon r_1(T_0, T_1, T_2) + \epsilon^2 r_2(T_0, T_1, T_2). \quad (27)$$

Substituting Eq. (27) into Eq. (26), collecting the coefficients of like powers of  $\epsilon$ , and equating each to zero, we obtain the following:

$$\mathcal{O}(\epsilon^0) : D_0^2 r_0(T_0, T_1, T_2) + \omega_0^2 r_0(T_0, T_1, T_2) = 0, \quad (28)$$

$$\begin{aligned} \mathcal{O}(\epsilon^1) : & D_0^2 r_1(T_0, T_1, T_2) + \omega_0^2 r_1(T_0, T_1, T_2) + 2\mu_1 D_0 r_0(T_0, T_1, T_2) \\ & + \mu_3 [D_0 r_0(T_0, T_1, T_2)]^3 + 2D_0 D_1 r_0(T_0, T_1, T_2) + \alpha_3 r_0(T_0, T_1, T_2)^3 \\ & + \alpha_5 r_0(T_0, T_1, T_2)^5 + kr_0(T_0 - \tau, T_1, T_2) - f \cos(\omega_0 T_0 + \sigma T_1) = 0, \end{aligned} \quad (29)$$

$$\begin{aligned}
\mathcal{O}(\epsilon^2) : & D_0^2 r_2(T_0, T_1, T_2) + \omega_0^2 r_2(T_0, T_1, T_2) + 2D_0 D_1 r_1(T_0, T_1, T_2) + 2D_0 D_2 r_0(T_0, T_1, T_2) \\
& + D_1^2 r_0(T_0, T_1, T_2) + 2\mu_1 [D_0 r_1(T_0, T_1, T_2) + D_1 r_0(T_0, T_1, T_2)] \\
& + 3\mu_3 [D_0 r_0(T_0, T_1, T_2)]^2 [D_0 r_1(T_0, T_1, T_2) + D_1 r_0(T_0, T_1, T_2)] \\
& + 3\alpha_3 [r_0(T_0, T_1, T_2)]^2 r_1(T_0, T_1, T_2) + 5\alpha_5 [r_0(T_0, T_1, T_2)]^4 r_1(T_0, T_1, T_2) \\
& - k\tau D_2 r_0(T_0 - \tau, T_1, T_2) + kr_1(T_0 - \tau, T_1, T_2) = 0,
\end{aligned} \tag{30}$$

where  $D_n \triangleq \partial/\partial T_n$ . The solution of Eq. (28) can be expressed in the following form:

$$r_0(T_0, T_1, T_2) = A(T_1, T_2) \cos(\omega_0 T_0) + B(T_1, T_2) \sin(\omega_0 T_0). \tag{31}$$

The functions  $A(T_1, T_2)$  and  $B(T_1, T_2)$  are arbitrary for this approximation and are determined by applying the solvability conditions (i.e., eliminating the secular terms) on the next-order approximation. Substituting Eq. (31) into Eq. (29), we obtain the following:

$$\begin{aligned}
& D_0^2 r_1(T_0, T_1, T_2) + \omega_0^2 r_1(T_0, T_1, T_2) + P_1 \cos(\omega_0 T_0) + P_2 \sin(\omega_0 T_0) \\
& + P_3 \cos(3\omega_0 T_0) + P_4 \sin(3\omega_0 T_0) + P_5 \cos(5\omega_0 T_0) + P_6 \sin(5\omega_0 T_0) = 0.
\end{aligned} \tag{32}$$

In Eq. (32), the variables  $P_i$  are given as follows:

$$P_1 = \frac{5}{8}\alpha_5 A^5 + \left(\frac{5}{4}\alpha_5 B^2 + \frac{3}{4}\alpha_3\right)A^3 + \frac{3}{4}\mu_3\omega_0^3 BA^2 + \left(\frac{5}{8}\alpha_5 B^4 + \frac{3}{4}\alpha_3 B^2 + k \cos(\omega_0\tau)\right)A + \frac{3}{4}\mu_3\omega_0^3 B^3 + [2\mu_1\omega_0 - k \sin(\omega_0\tau)]B + 2\omega_0 D_1 B - f \cos(\sigma T_1), \quad (33a)$$

$$P_2 = \frac{5}{8}\alpha_5 B^5 + \left(\frac{5}{4}\alpha_5 A^2 + \frac{3}{4}\alpha_3\right)B^3 - \frac{3}{4}\mu_3\omega_0^3 AB^2 + \left(\frac{5}{8}\alpha_5 A^4 + \frac{3}{4}\alpha_3 A^2 + k \cos(\omega_0\tau)\right)B - \frac{3}{4}\mu_3\omega_0^3 A^3 - [2\mu_1\omega_0 - k \sin(\omega_0\tau)]A - 2\omega_0 D_1 A + f \sin(\sigma T_1), \quad (33b)$$

$$P_3 = \frac{5}{16}\alpha_5 A^5 - \left(\frac{5}{8}\alpha_5 B^2 - \frac{1}{4}\alpha_3\right)A^3 - \frac{3}{4}\mu_3\omega_0^3 BA^2 - \left(\frac{15}{16}\alpha_5 B^2 + \frac{3}{4}\alpha_3\right)B^2 A + \frac{1}{4}\mu_3\omega_0^3 B^3, \quad (33c)$$

$$P_4 = -\frac{5}{16}\alpha_5 B^5 + \left(\frac{5}{8}\alpha_5 A^2 - \frac{1}{4}\alpha_3\right)B^3 - \frac{3}{4}\mu_3\omega_0^3 AB^2 + \left(\frac{15}{16}\alpha_5 A^2 + \frac{3}{4}\alpha_3\right)A^2 B + \frac{1}{4}\mu_3\omega_0^3 A^3, \quad (33d)$$

$$P_5 = \frac{1}{16}\alpha_5 A^5 - \frac{5}{8}\alpha_5 B^2 A^3 + \frac{5}{16}\alpha_5 B^4 A, \quad (33e)$$

$$P_6 = \frac{1}{16}\alpha_5 B^5 - \frac{5}{8}\alpha_5 A^2 B^3 + \frac{5}{16}\alpha_5 A^4 B, \quad (33f)$$

where  $A(T_1, T_2)$  and  $B(T_1, T_2)$  have been replaced with  $A$  and  $B$ , respectively.  $D_1 A$  and  $D_1 B$  can be obtained by solving  $P_1 = 0$  and  $P_2 = 0$ :

$$\begin{aligned} \frac{\partial A}{\partial T_1} = & \frac{1}{16\omega_0} \left\{ 5\alpha_5 B^5 + (10\alpha_5 A^2 + 6\alpha_3) B^3 - 6\mu_3\omega_0^3 AB^2 + [5\alpha_5 A^4 + 6\alpha_3 A^2 + 8k \cos(\omega_0\tau)] B \right. \\ & \left. - 6\mu_3\omega_0^3 A^3 - [16\mu_1\omega_0 - 8k \sin(\omega_0\tau)] A + 8f \sin(\sigma T_1) \right\}, \end{aligned} \quad (34a)$$

$$\begin{aligned} \frac{\partial B}{\partial T_1} = & \frac{-1}{16\omega_0} \left\{ 5\alpha_5 A^5 + (10\alpha_5 B^2 + 6\alpha_3) A^3 + 6\mu_3\omega_0^3 BA^2 + [5\alpha_5 B^4 + 6\alpha_3 B^2 + 8k \cos(\omega_0\tau)] A \right. \\ & \left. + 6\mu_3\omega_0^3 B^3 + [16\mu_1\omega_0 - 8k \sin(\omega_0\tau)] B - 8f \cos(\sigma T_1) \right\}. \end{aligned} \quad (34b)$$

The particular solution of Eq. (32) can be assumed to be of the following form:

$$r_1(T_0, T_1, T_2) = Q_1 \cos(3\omega_0 T_0) + Q_2 \sin(3\omega_0 T_0) + Q_3 \cos(5\omega_0 T_0) + Q_4 \sin(5\omega_0 T_0), \quad (35)$$

where  $Q_i \triangleq Q_i(T_1, T_2)$ . Substituting Eq. (35) into Eq. (32) and equating the coefficients of sine

and cosine to zero, we obtain the following expressions for each  $Q_i$ :

$$Q_1 = \frac{1}{128\omega_0^2} [5\alpha_5 A^5 - (10\alpha_5 B^2 - 4\alpha_3) A^3 - 12\mu_3\omega_0^3 B A^2 - (15\alpha_5 B^2 + 12\alpha_3) B^2 A + 4\mu_3\omega_0^3 B^3], \quad (36a)$$

$$Q_2 = \frac{-1}{128\omega_0^2} [5\alpha_5 B^5 - (10\alpha_5 A^2 - 4\alpha_3) B^3 + 12\mu_3\omega_0^3 A B^2 - (15\alpha_5 A^2 + 12\alpha_3) A^2 B - 4\mu_3\omega_0^3 A^3], \quad (36b)$$

$$Q_3 = \frac{\alpha_5 A}{384\omega_0^2} (5B^4 - 10A^2B^2 + A^4), \quad (36c)$$

$$Q_4 = \frac{\alpha_5 B}{384\omega_0^2} (5A^4 - 10B^2A^2 + B^4). \quad (36d)$$

Substituting Eqs. (31) and (35) into Eq. (30), setting the secular terms to zero, and solving the resulting equations, we obtain  $\partial A / \partial T_2$  and  $\partial B / \partial T_2$ . These expressions are lengthy and are omitted here for brevity. The above procedure can be continued down to any desired order.

The equations to compute the time derivatives of  $A$  and  $B$  are given as follows:

$$\frac{dA}{dt} = \epsilon \frac{\partial A}{\partial T_1} + \epsilon^2 \frac{\partial A}{\partial T_2} + \mathcal{O}(\epsilon^3), \quad (37a)$$

$$\frac{dB}{dt} = \epsilon \frac{\partial B}{\partial T_1} + \epsilon^2 \frac{\partial B}{\partial T_2} + \mathcal{O}(\epsilon^3). \quad (37b)$$

To simplify Eq. (37), we express  $A$  and  $B$  in polar coordinates:

$$A(T_1, T_2) = a(t) \sin(\beta(t)), \quad (38a)$$

$$B(T_1, T_2) = a(t) \cos(\beta(t)). \quad (38b)$$

Solving for  $\dot{a}(t)$  and  $\dot{\beta}(t)$ , we obtain the following:

$$\dot{a} = -\frac{3}{8}\hat{\mu}_3\omega_0^2 a^3 + \frac{1}{2}\hat{k}_p \sin(\omega_0\tau)a - \hat{\mu}_1 a + \frac{\hat{f}}{2\omega_0} \cos(\sigma T_1 - \beta) + \mathcal{O}(\epsilon^2), \quad (39a)$$

$$\dot{\beta} = \frac{1}{2\omega_0} \left( \frac{5}{8}\hat{\alpha}_5 a^4 + \frac{3}{4}\hat{\alpha}_3 a^2 + \hat{k}_p \cos(\omega_0\tau) + \frac{\hat{f}}{a} \sin(\sigma T_1 - \beta) \right) + \mathcal{O}(\epsilon^2), \quad (39b)$$

where  $a \triangleq a(t)$  and  $\beta \triangleq \beta(t)$  for brevity. Defining  $\gamma \triangleq \sigma T_1 - \beta$ , we have the following:

$$\dot{a} = -\frac{3}{8}\hat{\mu}_3\omega_0^2a^3 + \frac{1}{2}\hat{k}_p \sin(\omega_0\tau)a - \hat{\mu}_1a + \frac{\hat{f}}{2\omega_0} \cos(\gamma), \quad (40a)$$

$$a\dot{\gamma} = \sigma a - \frac{1}{2\omega_0} \left( \frac{5}{8}\hat{\alpha}_5a^5 + \frac{3}{4}\hat{\alpha}_3a^3 + \hat{k}_p \cos(\omega_0\tau)a + \hat{f} \sin(\gamma) \right). \quad (40b)$$

The steady-state response corresponds to  $\dot{a} = \dot{\gamma} = 0$ :

$$-\frac{3}{8}\hat{\mu}_3\omega_0^2a^3 + \frac{1}{2}\hat{k}_p \sin(\omega_0\tau)a - \hat{\mu}_1a + \frac{\hat{f}}{2\omega_0} \cos(\gamma) = 0, \quad (41a)$$

$$\sigma a - \frac{1}{2\omega_0} \left( \frac{5}{8}\hat{\alpha}_5a^5 + \frac{3}{4}\hat{\alpha}_3a^3 + \hat{k}_p \cos(\omega_0\tau)a + \hat{f} \sin(\gamma) \right) = 0. \quad (41b)$$

Finally, the frequency response equation is obtained upon eliminating  $\gamma$ :

$$a^2 \left( 3\hat{\mu}_3\omega_0^3a^2 - 4\hat{k}_p \sin(\omega_0\tau) + 8\hat{\mu}_1\omega_0 \right)^2 + \frac{a^2}{4} \left( 5\hat{\alpha}_5a^4 + 6\hat{\alpha}_3a^2 + 8\hat{k}_p \cos(\omega_0\tau) - 16\omega_0\sigma \right)^2 - 16\hat{f}^2 = 0. \quad (42)$$

We have presented the derivation for only the first-order approximation. The expressions are too lengthy to include here, but results will be presented for up to the second-order approximation. The MMS method provides reliable results at low amplitudes but not at high amplitudes; high-amplitude responses are analyzed using the harmonic balance method, which we present in the next section. To identify stable and unstable fixed points, we first use the spectral Tau method [36] to convert the DDE into a set of ordinary differential equations (ODEs), then apply Floquet theory.

## 7 Forced Response using Harmonic Balance

The harmonic balance method can be used to study the steady-state response of a nonlinear system by assuming a solution up to a finite number of harmonics [34]. An assumed solution is substituted into the equations governing the dynamics of the system; the equations are then solved for the unknown amplitudes by equating the coefficient of each harmonic to zero. This technique can

often provide an accurate approximation of the solution even if only a few harmonics are used.

Here, we proceed with a simple two-term approximation with a single harmonic:

$$r_0(t) = A \cos(\omega_e t) + B \sin(\omega_e t). \quad (43)$$

Substituting Eq. (43) into Eq. (26) and separating the coefficients of  $\cos(\omega_e t)$  and  $\sin(\omega_e t)$ , we obtain the following:

$$\begin{aligned} \frac{5}{8}\hat{\alpha}_5 A^5 + \left( \frac{5}{4}\hat{\alpha}_5 B^2 + \frac{3}{4}\hat{\alpha}_3 \right) A^3 + \frac{3}{4}\hat{\mu}_3 \omega_e^3 B A^2 + \left( \frac{5}{8}\hat{\alpha}_5 B^4 + \frac{3}{4}\hat{\alpha}_3 B^2 + \omega_0^2 - \omega_e^2 + k \cos(\omega_e \tau) \right) A \\ + \frac{3}{4}\hat{\mu}_3 \omega_e^3 B^3 + [2\hat{\mu}_1 \omega_e - k \sin(\omega_e \tau)] B - \frac{4}{5}F \omega_e = 0, \end{aligned} \quad (44a)$$

$$\begin{aligned} \frac{5}{8}\hat{\alpha}_5 B^5 + \left( \frac{5}{4}\hat{\alpha}_5 A^2 + \frac{3}{4}\hat{\alpha}_3 \right) B^3 - \frac{3}{4}\hat{\mu}_3 \omega_e^3 A B^2 + \left( \frac{5}{8}\hat{\alpha}_5 A^4 + \frac{3}{4}\hat{\alpha}_3 A^2 + \omega_0^2 - \omega_e^2 + k \cos(\omega_e \tau) \right) B \\ - \frac{3}{4}\hat{\mu}_3 \omega_e^3 A^3 - [2\hat{\mu}_1 \omega_e - k \sin(\omega_e \tau)] A = 0. \end{aligned} \quad (44b)$$

We use the pseudo-arc-length continuation method [10] to solve Eq. (44) for  $A$  and  $B$ . Next, we express  $r_0(t)$  from Eq. (43) in polar form:

$$r_0(t) = R \cos(\omega_e t - \phi), \quad (45)$$

where  $R = \sqrt{A^2 + B^2}$  and  $\phi = \arctan(B, A)$ . We perturb the steady-state solution from  $r_0(t)$  (i.e., we let  $r(t) = r_0(t) + \delta(t)$ ) to determine whether the system behaviour is stable or unstable in response to a disturbance. Linearizing Eq. (26) around  $r_0(t)$ , we have the following:

$$\ddot{\delta}(t) + [2\hat{\mu}_1 + 3\hat{\mu}_3 r_0^2(t)] \dot{\delta}(t) + [5\hat{\alpha}_5 r_0^4(t) + 3\hat{\alpha}_3 r_0^2(t) + \omega_0^2] \delta(t) + k\delta(t - \tau) = 0. \quad (46)$$

Equation (46) is a linear second-order DDE with periodic coefficients. We convert Eq. (46) into a set of ODEs with periodic coefficients using the spectral Tau method. We then apply Floquet theory with a period of  $\pi/\omega_e$  to determine the nature of the limit cycle. This procedure has been described in Appendices A and B; additional details can be found in the literature [35].

The global bifurcation diagrams in the plane of the excitation amplitude ( $a^*$ ) and excitation frequency ( $\sigma$ ) are shown for the low- and medium-freeboard models in Fig. 7. Three wave slopes

$(F)$  are considered in each case. The “dde23” solver in MATLAB<sup>®</sup> is used to solve Eq. (26) to obtain the time response of the forced system, with absolute and relative tolerances set to  $10^{-6}$ . Zero displacement and zero velocity are used as the history functions. The maximum amplitude of the steady-state response obtained from the “dde23” solution in each condition is indicated by circles in Fig. 7. The implicit function given by Eq. (42) is solved to obtain the MMS response, shown as triangles in Fig. 7. The steady-state amplitudes obtained using the MMS approach agree with those obtained from the “dde23” solution at low wave slopes. The amplitudes calculated from the harmonic balance method (Eq. (45)) are shown as solid blue lines (stable limit cycles) and red dots (unstable limit cycles) in Fig. 7. The stability of the limit cycles is determined from Eq. (46) following application of the spectral Tau method and Floquet theory. In contrast to the MMS approach, the harmonic balance method agrees with the “dde23” solution even at higher wave slopes. As can be seen in Fig. 7 for both ship models, the peaks in the relative roll motion shift toward lower frequencies as the wave slope increases.

The forced responses of the low- and medium-freeboard models with and without an ART are shown in Fig. 8. As illustrated, the proposed ART control system effectively reduces peak roll amplitudes. Figure 9 compares the forced response of the system when the optimal proportional gain is used but where the delay ( $\tau$ ) and wave slope ( $F$ ) vary. We observe that the optimal delay found previously ( $\tau = 0.87$  s) outperforms delays of  $\tau = 0.7$  s and  $\tau = 1$  s. Thus, we verify that linear stability analysis and the spectral Tau method can be used to obtain the optimal proportional gain and delay parameters for the controller, which may be preferable to a trial-and-error-based approach.

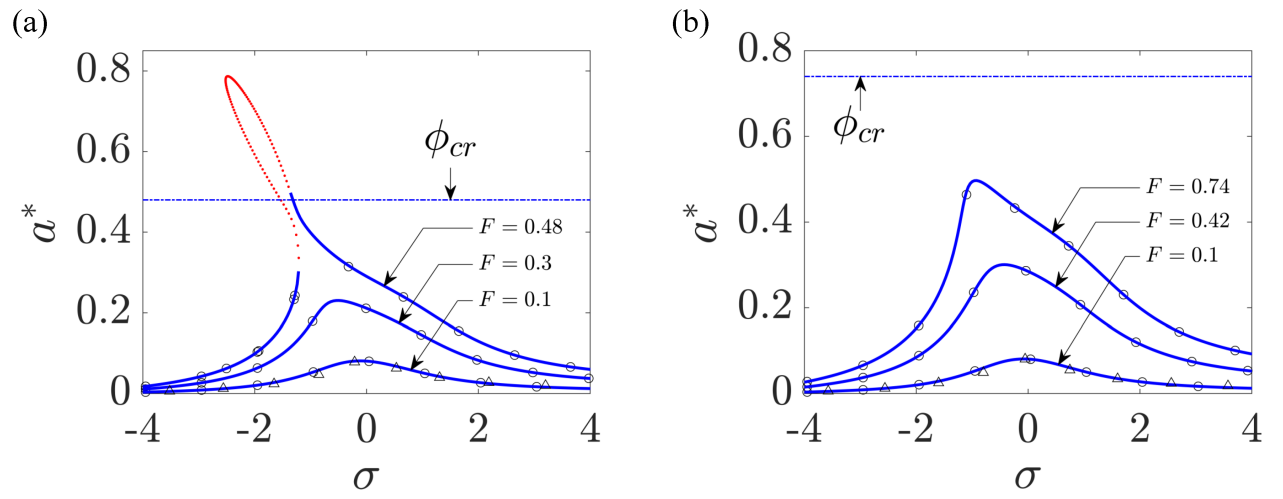


**Figure 7:** Global bifurcation diagram in the plane of the excitation amplitude  $a^*$  and excitation frequency  $\sigma$  for (a) low-freeboard and (b) medium-freeboard models. Circles: “dde23” solution; triangles: MMS approach; solid blue lines and red dots: respectively, stable and unstable limit cycles from harmonic balance method;  $\phi_{cr}$ : critical roll angle, or maximum static roll angle before capsizing.

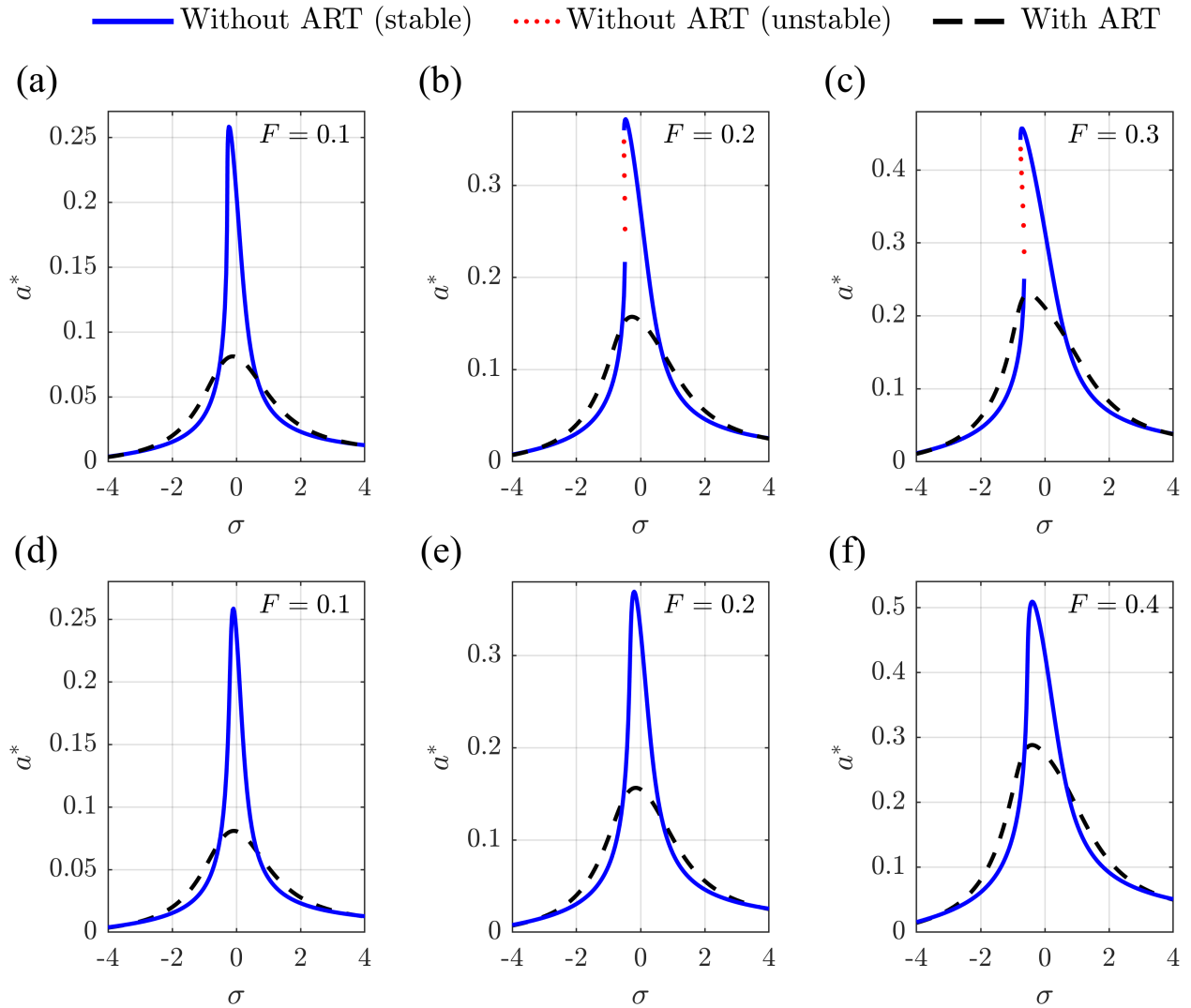


**Figure 8:** Global bifurcation diagrams in the plane of the excitation amplitude  $a^*$  and excitation frequency  $\sigma$  with and without ART for different wave slope  $F$ , generated using the harmonic balance method: (a–c) low-freeboard and (d–f) medium-freeboard models. Solid blue lines and red dots: respectively, stable and unstable limit cycles without ART; dashed black lines: stable limit cycles with ART.

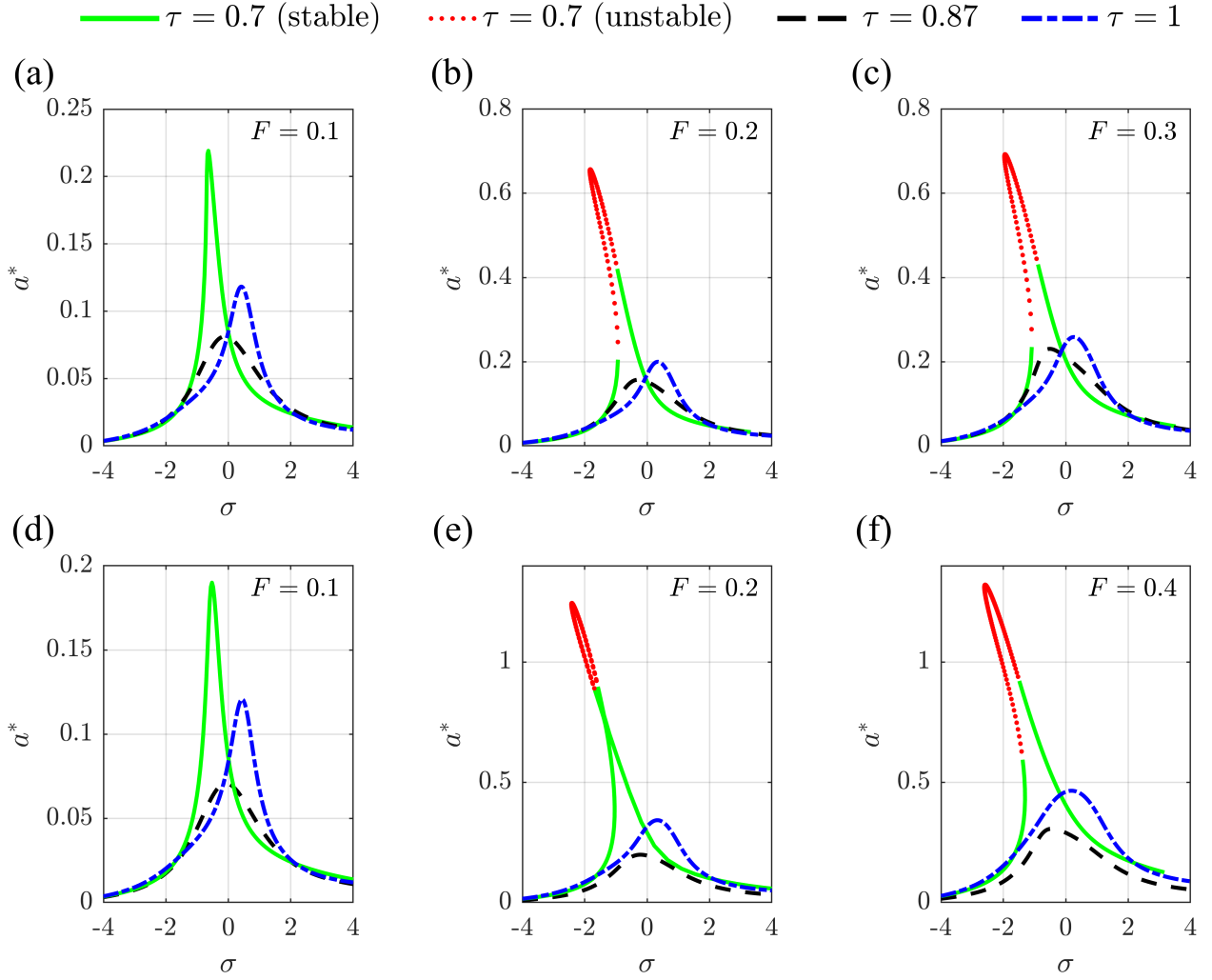


**Figure 9:** Global bifurcation diagrams in the plane of the excitation amplitude  $a^*$  and excitation frequency  $\sigma$  for different wave slope  $F$  and delay  $\tau$ , generated using the harmonic balance method: (a–c) low-freeboard and (d–f) medium-freeboard models. Solid green lines, dashed black lines, and dash-dotted blue lines: stable limit cycles for  $\tau = 0.7$  s,  $\tau = 0.87$  s, and  $\tau = 1$  s, respectively; red dots: unstable limit cycles.

## 8 Conclusions

A dynamic analysis has been performed for a harmonically excited single-degree-of-freedom system with cubic and quintic nonlinearities and a proportional-gain controller with constant delay. This system represents the roll dynamics of a ship under control of an active U-tube anti-roll tank. The delay in this system manifests from the time required to pump fluid between tanks on the port side and starboard side of the ship, the inertia associated with large impellers and linkages, and the sensing and processing time of the controller. Linear stability analysis and the spectral Tau method were used to obtain the optimal proportional gain and delay in closed form, which offers clear benefits over traditional trial-and-error and optimization strategies. These analyses were shown to be effective for low- and medium-freeboard ship models but not a high-freeboard model as the latter did not have a region of zero equilibrium within the operating region. We concluded from the linear stability analysis that derivative control is always detrimental for this system. Closed-form solutions were obtained at the supercritical Hopf bifurcation points using the method of multiple scales in a local bifurcation analysis. A global bifurcation analysis revealed the existence of high-amplitude limit cycles along with a stable zero equilibrium in the pre-bifurcation regime, and period-doubling limit-cycle oscillations in the post-bifurcation regime.

The response of the harmonically excited system with optimal proportional-gain and delay control parameters was studied. The delayed proportional controller prevented the ship from undergoing high-amplitude period-doubling oscillations (capsizing limit cycles) at high wave slopes. The method of multiple scales was used to obtain closed-form solutions at low wave slopes; the harmonic balance approach was used for higher wave slopes. The spectral Tau method and Floquet theory were applied to distinguish between stable and unstable limit cycles. The presented analytical results were verified by direct numerical simulations.

The key findings of this study are twofold. First, our free-vibration analysis revealed the exis-

tence of multiple solutions. Notably, a large-amplitude limit cycle can be reached if a sufficiently large disturbance is encountered, such as from a rogue wave, even in the pre-bifurcation regime (i.e., for  $\epsilon\delta < 0$  in Figs. 5 and 6). The second key finding is that smaller control delay  $\tau$  is not always better: in some cases, reducing  $\tau$  will reduce the maximum gain for which the system will be stable (see Fig. 2). Thus, in practice, it may be necessary to tune the gains as well as the delay of the controller. The analyses presented in this work can be applied to determine control parameters and the power requirements for pumps in active anti-roll tanks. Directions for future work include identifying optimal control parameters for the high-freeboard ship model, studying double Hopf bifurcation points in the  $[\hat{k}_p, \tau]$  space, and experimentally validating the efficacy of the computed parameters at controlling the parametric resonance of ships.

## Funding Statement

This work was partially supported by the National Board of Higher Mathematics (project number 02011/2/2021/NBHM(R.P)/R&D II/3628). The funders had no role in study design, data collection and analysis, decision to publish, or preparation of the manuscript.

## References

- [1] Zhou, B., Qi, X., Zhang, J., and Zhang, H., 2021. “Effect of 6-DOF oscillation of ship target on SAR imaging”. *Remote Sens*, **13**(9), p. 1821. doi:10.3390/rs13091821.
- [2] Molnar, T. G., Dombovari, Z., Insperger, T., and Stepan, G., 2017. “On the analysis of the double Hopf bifurcation in machining processes via centre manifold reduction”. *Proc R Soc A*, **473**(2207), p. 20170502. doi:10.1098/rspa.2017.0502.

- [3] Beregi, S., Takacs, D., and Stepan, G., 2019. “Bifurcation analysis of wheel shimmy with non-smooth effects and time delay in the tyre–ground contact”. *Nonlinear Dyn*, **98**(1), pp. 841–858. doi:10.1007/s11071-019-05123-1.
- [4] Zhang, L., and Stepan, G., 2020. “Bifurcations in basic models of delayed force control”. *Nonlinear Dyn*, **99**(1), pp. 99–108. doi:10.1007/s11071-019-05058-7.
- [5] Nayfeh, A. H., and Khdeir, A. A., 1986. “Nonlinear rolling of ships in regular beam seas”. *Int Shipbuild Prog*, **33**(379), pp. 40–49. doi:10.3233/ISP-1986-3337901.
- [6] Nayfeh, A. H., and Khdeir, A. A., 1986. “Nonlinear rolling of biased ships in regular beam waves”. *Int Shipbuild Prog*, **33**(381), pp. 84–93. doi:10.3233/ISP-1986-3338102.
- [7] Thompson, J. M. T., Rainey, R. C. T., and Soliman, M. S., 1992. “Mechanics of ship capsize under direct and parametric wave excitation”. *Philos Trans A Math Phys Eng Sci*, **338**(1651), pp. 471–490. doi:10.1098/rsta.1992.0015.
- [8] Thompson, J. M. T., and Stewart, H. B., 2002. *Nonlinear Dynamics and Chaos*, 2nd ed. John Wiley & Sons, Chichester, England.
- [9] Senjanović, I., Parunov, J., and Ciprić, G., 1997. “Safety analysis of ship rolling in rough sea”. *Chaos Solitons Fractals*, **8**(4), pp. 659–680. doi:10.1016/S0960-0779(96)00114-2.
- [10] Spyrou, K. J., and Thompson, J. M. T., 2000. “The nonlinear dynamics of ship motions: a field overview and some recent developments”. *Philos Trans A Math Phys Eng Sci*, **358**(1771), pp. 1735–1760. doi:10.1098/rsta.2000.0613.
- [11] Spyrou, K. J., 2005. “Design criteria for parametric rolling”. *Ocean Eng Int*, **9**(1), pp. 11–27.
- [12] Ibrahim, R. A., and Grace, I. M., 2010. “Modeling of ship roll dynamics and its coupling with heave and pitch”. *Math Probl Eng*, **2010**, p. 934714. doi:10.1155/2010/934714.

- [13] Neves, M. A. S., 2016. “Dynamic stability of ships in regular and irregular seas – An overview”. *Ocean Eng*, **120**, pp. 362–370. doi:10.1016/j.oceaneng.2016.02.010.
- [14] Froude, W., 1874. “Considerations respecting the rolling of ships at sea”. *Trans Inst Nav Archit*, **14**, pp. 96–116.
- [15] Watts, P., 1885. “The use of water chambers for reducing the rolling of ships at sea”. *Trans Inst Nav Archit*, **26**, p. 30.
- [16] Frahm, H. H., 1911. “Results of trials of the anti-rolling tanks at sea”. *J Am Soc Nav Eng*, **23**(2), pp. 571–597. doi:10.1111/j.1559-3584.1911.tb04595.x.
- [17] Minorsky, N., 1935. “Problems of anti-rolling stabilization of ships by the activated tank method”. *J Am Soc Nav Eng*, **47**(1), pp. 87–119. doi:10.1111/j.1559-3584.1935.tb04304.x.
- [18] Minorsky, N., 1941. “Note on the angular motions of ships”. *J Appl Mech*, **8**(3), pp. A111–A120. doi:10.1115/1.4009116.
- [19] Chadwick, J. H., and Klotter, K., 1954. “On the dynamics of anti-roll tanks”. *Schiffstechnik*, **2**, pp. 23–45.
- [20] Stigter, C., 1966. “The performance of U-tanks as a passive anti-rolling device”. *Int Shipbuild Prog*, **13**(144), pp. 249–275. doi:10.3233/ISP-1966-1314401.
- [21] Van den Bosch, J. J., and Vugts, J. H., 1966. “On roll damping by free-surface tanks”. *Trans R Inst Nav Archit*, **108**, pp. 345–361.
- [22] Abdel Gawad, A. F., Ragab, S. A., Nayfeh, A. H., and Mook, D. T., 2001. “Roll stabilization by anti-roll passive tanks”. *Ocean Eng*, **28**(5), pp. 457–469. doi:10.1016/S0029-8018(00)00015-9.

- [23] Youssef, K. S., Ragab, S. A., Nayfeh, A. H., and Mook, D. T., 2002. “Design of passive anti-roll tanks for roll stabilization in the nonlinear range”. *Ocean Eng*, **29**(2), pp. 177–192. doi:10.1016/S0029-8018(01)00021-X.
- [24] Youssef, K. S., Mook, D. T., Nayfeh, A. H., and Ragab, S. A., 2003. “Roll stabilization by passive anti-roll tanks using an improved model of the tank-liquid motion”. *J Vib Control*, **9**(7), pp. 839–862. doi:10.1177/1077546303009007006.
- [25] Marzouk, O. A., and Nayfeh, A. H., 2009. “Control of ship roll using passive and active anti-roll tanks”. *Ocean Eng*, **36**(9–10), pp. 661–671. doi:10.1016/j.oceaneng.2009.03.005.
- [26] Moaleji, R., and Greig, A. R., 2007. “On the development of ship anti-roll tanks”. *Ocean Eng*, **34**(1), pp. 103–121. doi:10.1016/j.oceaneng.2005.12.013.
- [27] Vugts, J. H., 1969. “A comparative study on four different passive roll damping tanks”. *Int Shipbuild Prog*, **16**(179), pp. 212–223. doi:10.3233/ISP-1969-1617903.
- [28] Shin, Y. S., Belenky, V. L., Lin, W. M., Weems, K. M., and Engle, A. H., 2003. “Nonlinear time domain simulation technology for seakeeping and wave-load analysis for modern ship design”. *Trans Soc Nav Archit Mar Eng*, **111**, pp. 557–583.
- [29] Phairoh, T., and Huang, J.-K., 2005. “Modeling and analysis of ship roll tank stimulator systems”. *Ocean Eng*, **32**(8–9), pp. 1037–1053. doi:10.1016/j.oceaneng.2004.09.007.
- [30] Alujević, N., Ćatipović, I., Malenica, Š., Senjanović, I., and Vladimir, N., 2019. “Ship roll control and power absorption using a U-tube anti-roll tank”. *Ocean Eng*, **172**, pp. 857–870. doi:10.1016/j.oceaneng.2018.12.007.

- [31] Kučera, V., Pilbauer, D., Vyhlídal, T., and Olgac, N., 2017. “Extended delayed resonators – design and experimental verification”. *Mechatronics*, **41**, pp. 29–44. doi:10.1016/j.mechatronics.2016.10.019.
- [32] Spyrou, K. J., 1999. “On course-stability and control delay”. *Int Shipbuild Prog*, **46**(448), pp. 421–443.
- [33] Nayfeh, A. H., 2004. *Introduction to Perturbation Techniques*. Wiley-VCH, Weinheim, Germany.
- [34] Mickens, R. E., 2010. *Truly Nonlinear Oscillations: Harmonic Balance, Parameter Expansions, Iteration, and Averaging Methods*. World Scientific, Singapore.
- [35] Kuznetsov, Y., 2004. *Elements of Applied Bifurcation Theory*, 3rd ed. Springer-Verlag, New York, NY, USA. doi:10.1007/978-1-4757-3978-7.
- [36] Vyasarayani, C. P., Subhash, S., and Kalmár-Nagy, T., 2014. “Spectral approximations for characteristic roots of delay differential equations”. *Int J Dyn Control*, **2**(2), pp. 126–132. doi:10.1007/s40435-014-0060-2.
- [37] Wright, J. H. G., and Marshfield, W. B., 1980. “Ship roll response and capsizing behaviour in beam seas”. *Trans R Inst Nav Archit*, **122**, pp. 129–148.
- [38] Insperger, T., and Stépán, G., 2011. *Semi-Discretization for Time-Delay Systems: Stability and Engineering Applications*. Springer, New York, NY, USA. doi:10.1007/978-1-4614-0335-7.
- [39] Campbell, S. A., Bélair, J., Ohira, T., and Milton, J., 1995. “Complex dynamics and multistability in a damped harmonic oscillator with delayed negative feedback”. *Chaos Interdiscip J Nonlinear Sci*, **5**(4), pp. 640–645. doi:10.1063/1.166134.

- [40] Das, S. L., and Chatterjee, A., 2002. “Multiple scales without center manifold reductions for delay differential equations near Hopf bifurcations”. *Nonlinear Dyn*, **30**(4), pp. 323–335.  
doi:10.1023/A:1021220117746.

## A Spectral Tau Method

Consider a delay differential equation with a time-periodic coefficient and a constant delay  $\tau$ :

$$\dot{x}(t) = a(t)x(t) + cx(t - \tau), \quad (47)$$

where  $a(t+T) = a(t)$  and  $c \in \mathbb{R}$ . We define the transformation  $y(s, t) = x(t+s)$  with  $-\tau \leq s \leq 0$ , whereupon the initial-value problem is converted into the following boundary-value problem:

$$\frac{\partial y(s, t)}{\partial t} = \frac{\partial y(s, t)}{\partial s}, \quad (48)$$

$$\left. \frac{\partial y(s, t)}{\partial t} \right|_{s=0} = a(t)y(0, t) + cy(-\tau, t), \quad (49)$$

$$y(s, 0) = \gamma(s), \quad (50)$$

where  $\gamma(s)$  is the history function. The solution to the partial differential equation (Eq. (48)) is assumed to be of the following form:

$$y(s, t) = \sum_{i=1}^{\infty} \theta_i(s)\eta_i(t), \quad (51)$$

where  $\theta_i(s)$  are the basis functions. We truncate the infinite series in Eq. (51) to  $N$  terms:

$$y(s, t) = \boldsymbol{\theta}^T(s)\boldsymbol{\eta}(t), \quad (52)$$

where  $\boldsymbol{\theta}(s) = [\theta_1(s), \theta_2(s), \dots, \theta_N(s)]^T$  and  $\boldsymbol{\eta}(t) = [\eta_1(t), \eta_2(t), \dots, \eta_N(t)]^T$ . Upon substituting Eq. (52) into Eq. (48), we obtain the following:

$$\boldsymbol{\theta}^T(s)\dot{\boldsymbol{\eta}}(t) = (\boldsymbol{\theta}'(s))^T \boldsymbol{\eta}(t), \quad (53)$$

where  $\dot{\boldsymbol{\eta}}(t) \triangleq d\boldsymbol{\eta}(t)/dt$  and  $\boldsymbol{\theta}'(s) \triangleq d\boldsymbol{\theta}(s)/ds$ . Premultiplying Eq. (53) by  $\boldsymbol{\theta}(s)$  and integrating over the domain, we obtain the following equation in matrix form:

$$\mathbf{A}\dot{\boldsymbol{\eta}}(t) = \mathbf{B}\boldsymbol{\eta}(t), \quad (54)$$

where  $\mathbf{A} = \int_{-\tau}^0 \boldsymbol{\theta}(s)\boldsymbol{\theta}^T(s) ds$  and  $\mathbf{B} = \int_{-\tau}^0 \boldsymbol{\theta}(s)(\boldsymbol{\theta}'(s))^T ds$ . Substituting Eq. (52) into Eq. (49), we have

$$\boldsymbol{\theta}^T(0)\dot{\boldsymbol{\eta}}(t) = a(t)\boldsymbol{\theta}^T(0)\boldsymbol{\eta}(t) + c\boldsymbol{\theta}^T(-\tau)\boldsymbol{\eta}(t). \quad (55)$$

In total, Eqs. (54) and (55) comprise  $N + 1$  equations. To form a determinate system, we replace the last row in Eq. (54) with Eq. (55):

$$\mathbf{M}\dot{\boldsymbol{\eta}}(t) = \mathbf{K}\boldsymbol{\eta}(t), \quad (56)$$

where matrices  $\mathbf{M}$  and  $\mathbf{K}$  are given as follows:

$$\mathbf{M} = \begin{bmatrix} \bar{\mathbf{A}} \\ \boldsymbol{\theta}^T(0) \end{bmatrix}, \quad \mathbf{K} = \begin{bmatrix} \bar{\mathbf{B}} \\ a(t)\boldsymbol{\theta}^T(0) + c\boldsymbol{\theta}^T(-\tau) \end{bmatrix}. \quad (57)$$

In Eq. (57),  $\bar{\mathbf{A}}$  and  $\bar{\mathbf{B}}$  are the first  $N - 1$  rows of  $\mathbf{A}$  and  $\mathbf{B}$  from Eq. (54). Equation (56) can be rewritten as follows:

$$\dot{\boldsymbol{\eta}}(t) = \mathbf{F}(t)\boldsymbol{\eta}(t), \quad (58)$$

where  $\mathbf{F}(t) = \mathbf{M}^{-1}\mathbf{K}$  is time-periodic with period  $T$ . Initial conditions for solving Eq. (58) are obtained from Eqs. (50) and (52) at  $t = 0$ :

$$\boldsymbol{\eta}(0) = \mathbf{M}^{-1} \int_{-\tau}^0 \boldsymbol{\theta}^T(s)\gamma(s) ds. \quad (59)$$

Equations (58) and (59) can then be solved numerically to obtain the time response of the system (Eq. (47)).

## A.1 Stability analysis

The stability of the system described by Eq. (58) can be determined by analyzing  $\mathbf{F}(t)$ . If  $a(t)$  is not a periodic coefficient (i.e., it is simply a real number), then the eigenvalues of matrix  $\mathbf{F}$  determine the system's stability. If  $\mathbf{F}(t)$  is time-periodic (i.e.,  $\mathbf{F}(t + T) = \mathbf{F}(t)$ ), then we use Floquet theory (specifically, the eigenvalues of the Floquet transition matrix) to determine the stability of the system. The Floquet transition matrix  $\Phi(T)$  is defined as follows:

$$\boldsymbol{\eta}(T) = \Phi(T)\boldsymbol{\eta}(0). \quad (60)$$

If all eigenvalues of  $\Phi(T)$  have magnitude less than 1, then the system is stable; otherwise, it is unstable. The Floquet transition matrix can be calculated by solving the following initial-value problem, integrating to time  $t = T$ :

$$\dot{\Phi}(t) = \mathbf{F}(t)\Phi(t), \quad (61)$$

with initial condition  $\Phi(0) = \mathbf{I}$ .

## A.2 Basis functions

Various basis functions have been explored in the literature, including the mixed Fourier basis

$$\boldsymbol{\theta}(s) = \left[ 1, s, \sin\left(\frac{\pi s}{\tau}\right), \sin\left(\frac{2\pi s}{\tau}\right), \dots \right]^T, \quad (62)$$

shifted Legendre polynomials

$$\theta_1(s) = 1, \quad (63a)$$

$$\theta_2(s) = 1 + \frac{2s}{\tau}, \quad (63b)$$

$$\theta_i(s) = \frac{(2i-3)\theta_2(s)\theta_{i-1}(s) - (i-2)\theta_{i-2}(s)}{i-1}, \quad i \geq 3, \quad (63c)$$

and shifted Chebyshev polynomials

$$\theta_1(s) = 1, \quad (64a)$$

$$\theta_2(s) = 1 + \frac{2s}{\tau}, \quad (64b)$$

$$\theta_i(s) = 2\theta_2(s)\theta_{i-1}(s) - \theta_{i-2}(s), \quad i \geq 3. \quad (64c)$$

We use shifted Legendre polynomials as, with these basis functions, the mass and stiffness matrices in Eq. (54) can be simplified:

$$A_{ij} = \frac{\tau}{2i-1} \delta_{ij}, \quad (65a)$$

$$B_{ij} = \begin{cases} 0 & \text{if } i \geq j \\ 2 & \text{if } i < j \text{ and } i+j \text{ is odd} \\ 0 & \text{if } i < j \text{ and } i+j \text{ is even} \end{cases}, \quad (65b)$$

for  $i, j = 1, 2, \dots, N$ .

## B Pseudo-Arclength Continuation

Consider the following nonlinear algebraic equation:

$$\mathbf{f}(\mathbf{x}, \alpha) = 0, \quad (66)$$

where  $\mathbf{f} : \mathbb{R}^{N+1} \rightarrow \mathbb{R}^N$ ,  $\mathbf{x} \in \mathbb{R}^N$ , and  $\alpha \in \mathbb{R}$ . In other continuation techniques, parameter  $\alpha$  is continued to solve the system; however, in the pseudo-arclength continuation method, the parameter itself depends on the arclength  $s$ , and  $s$  is continued to solve the system:

$$\mathbf{f}(\mathbf{x}(s), \alpha(s), s) = 0. \quad (67)$$

If two points  $(\mathbf{x}_0^T, \alpha_0)$  and  $(\mathbf{x}_1^T, \alpha_1)$  are known, as well as a tangent vector  $\mathbf{t}_0$ , then we can use the total derivative of Eq. (67) to compute the tangent of the next iteration ( $\mathbf{t}_1$ ):

$$\begin{bmatrix} \mathbf{f}_x & \mathbf{f}_\alpha \end{bmatrix} \begin{Bmatrix} \dot{\mathbf{x}}_1 \\ \dot{\alpha}_1 \end{Bmatrix} = 0, \quad (68)$$

where  $\mathbf{f}_x = \partial \mathbf{f} / \partial \mathbf{x}$ ,  $\mathbf{f}_\alpha = \partial \mathbf{f} / \partial \alpha$ ,  $\dot{\mathbf{x}}_i = d\mathbf{x}_i/ds$ , and  $\dot{\alpha}_i = d\alpha_i/ds$ . The solution is then searched in the plane orthogonal to the tangent  $\mathbf{t}_1$ . The tangent predictor is defined as follows:

$$\mathbf{x}_2 = \mathbf{x}_1 + \dot{\mathbf{x}}_1 \Delta s, \quad (69a)$$

$$\alpha_2 = \alpha_1 + \dot{\alpha}_1 \Delta s. \quad (69b)$$

The orthogonality condition is given by

$$\mathbf{X}^T \mathbf{t}_1 = 0, \quad (70)$$

where  $\mathbf{X} = \begin{Bmatrix} \mathbf{x} - \mathbf{x}_2 \\ \alpha - \alpha_2 \end{Bmatrix}$  and  $\mathbf{t}_1 = \begin{Bmatrix} \dot{\mathbf{x}}_1 \\ \dot{\alpha}_1 \end{Bmatrix}$ . Solving Eq. (70) using Eqs. (68) and (69), we obtain the following condition:

$$(\mathbf{x} - \mathbf{x}_1) \dot{\mathbf{x}}_1 + (\alpha - \alpha_1) \dot{\alpha}_1 - \Delta s = 0. \quad (71)$$

Finally, Eqs. (67) and (71) form a system of  $N + 1$  equations, which can be solved using Newton–Raphson iteration upon selecting a small (arbitrary) value for  $\Delta s$ ; the Jacobian for this system is

$$J = \begin{bmatrix} \mathbf{f}_x & \mathbf{f}_\alpha \\ \dot{\mathbf{x}}_1 & \dot{\alpha}_1 \end{bmatrix}. \quad (72)$$